

A combination of Notch signaling, preferential adhesion and endocytosis induces a slow mode of cell intercalation in the *Drosophila* retina.

Laura Blackie^{1,2}, Melda Tozluoglu¹, Mateusz Trylinski^{1,3}, Rhian F. Walther¹, François Schweisguth^{3,5} Yanlan Mao^{1,4*} and Franck Pichaud^{1,4*}

¹ MRC Laboratory for Molecular Cell Biology (LMCB), University College London, London, United Kingdom.

² MRC London Institute of Medical Sciences (LMS), London, United Kingdom

³ Department of Developmental and Stem Cell Biology, Pasteur Institute, F-75015, Paris, France.

⁴ Institute for the Physics of Living Systems, University College London, London, United Kingdom.

⁵ CNRS, UMR3738, F-75015, Paris, France

* Corresponding authors: y.mao@ucl.ac.uk and f.pichaud@ucl.ac.uk

Phone: (+44) 0 207 679 7817

Fax: (+44) 0 207 679 7805

Abstract

Movement of epithelial cells in a tissue occurs through neighbor exchange and drives tissue shape changes. It requires intercellular junction remodeling, a process typically powered by the contractile actomyosin cytoskeleton. This has mostly been investigated in homogeneous epithelia where intercalation takes minutes. However, in some tissues, intercalation involves different cell types and can take hours. Whether slow and fast intercalation share the same mechanisms remains to be examined. To address this issue, we use the fly eye, where the cone cells exchange neighbors over approximately 10 hours to shape the lens. We uncover three pathways regulating this slow mode of cell intercalation. Firstly, we find a limited requirement for MyosinII. In this case, mathematical modeling predicts an adhesion dominant intercalation mechanism. Genetic experiments support this prediction and reveal a role for adhesion through the Nephtrin proteins Roughest and Hibris. Secondly, we find cone cell intercalation is regulated by the Notch-signaling pathway. Thirdly, we show endocytosis is required for membrane removal and Notch activation. Altogether, our work indicates that adhesion, endocytosis and Notch can induce junction remodeling over long-time scales.

INTRODUCTION

Epithelial cells are polarized along the apical (top)-basal (bottom) axis and assemble into tissues via their lateral Adherens Junctions (AJ). Loss and creation of AJs between cells can shape tissues by re-arranging the relative position of cells within the plane of the epithelium. For example, in the *Drosophila* germband, polarized steps of AJ loss and creation promote tissue elongation by inducing cell intercalation along the anterior-posterior axis of the embryo (Bertet et al., 2004; Blankenship et al., 2006; Tetley et al., 2016; Zallen and Wieschaus, 2004). Similar regulations take place between mesodermal cells in zebrafish to promote convergent extension (Yin et al., 2008), or during renal tube development in *Xenopus* for example (Lienkamp et al., 2012). In these relatively homogeneous tissues, intercalation between groups of four cells takes place over minutes.

In the germband, the RhoA-Rok-MyoII pathway controls actomyosin contractility, and Ecadherin (Ecad) mediates adhesion (Garcia De Las Bayonas et al., 2019; Levayer and Lecuit, 2013; Levayer et al., 2011; Munjal et al., 2015; Pare et al., 2014; Rauzi et al., 2010; Simoes Sde et al., 2010; Simoes Sde et al., 2014). Examining actomyosin dynamics in groups of four intercalating cells in this tissue shows that polarized actomyosin flows generate contractile forces that are harnessed by the junctional pool of actomyosin to remodel AJs between cells. Thus, MyoII accumulates preferentially at the AJs that shrink to drive intercalation. In this tissue, cell intercalation also requires endocytosis to shed membrane as an AJ is eliminated (Levayer et al., 2011). In other tissues such as the fly notum and wing disc, where cell intercalation also occurs over minutes, neighbor exchange is stochastic and reversible. Here, while MyoII is required for intercalation, its excessive accumulation at the AJ inhibits this intercalation (Curran et al., 2017). Furthermore, in the dorsal branch of the fly trachea, where cells intercalate to form tubes, MyoII is largely dispensable. In this case, intercalation between branch-cells is induced by forces

that are generated by the migrating tip-cell, which pulls on the branch cells (Ochoa-Espinosa et al., 2017). Importantly, these examples indicate that there is no simple relationship between MyoII and intercalation.

The fly ommatidium, which is the basic visual unit of the insect compound eye, presents an interesting departure point from all these tissues in that it includes a deterministic step of neighbor exchange between four cells, that unfolds over approximately 10 hours and that is very reproducible. This slow intercalation occurs during lens formation, between four epithelial-like cells, called the cone cells. Whether this type of slow intercalation is governed by the same mechanisms that underpin faster intercalation has not been investigated in detail. In the ommatidium, the four core cone cells are surrounded by two large primary pigment cells, themselves surrounded by a complement of narrow secondary and tertiary pigment cells – collectively referred to as Interommatidial cells (Cagan, 2009; Cagan and Ready, 1989; Charlton-Perkins et al., 2017; Ready et al., 1976; Wolff., 1993) (Figure 1A). As they are specified, each one of the cone and pigment cells finds their location in the 2D plane of the lens through highly regulated steps of neighbor exchange (Cagan and Ready, 1989; Larson et al., 2008). These steps of neighbor exchange are controlled by preferential adhesion, whereby adhesion is favored between the primary pigment cells and the interommatidial precursors and is minimized amongst interommatidial cells. This preferential adhesion relies on the Neph/Nephrin-like immunoglobulin adhesion protein family. Hbris (Hbs; Nephrin-like) is expressed in the primary pigment cells and binds to Roughest (Rst; Neph-1), which is expressed in the interommatidial precursors (Bao and Cagan, 2005). In addition, Hbs functions in the four core cone cells to regulate their intercalation (Grillo-Hill and Wolff, 2009), suggesting preferential adhesion might be involved in cone cell intercalation. However so far, no requirement for Rst has been found in these cells. In addition, Ncadherin (Ncad) has also been shown to play a role in regulating cone

cell intercalation through establishing a planar polarized pattern of interfacial tension within the cone cell quartet. In this pattern, a higher tension, generated by MyoII, is found at the interface between the cone and primary pigment cells, when compared to the AJs between the cone cells where MyoII tension is limited (Chan et al., 2017). However, how this MyoII pattern contributes to regulating intercalation in these cells and how it relates to preferential adhesion through Hbs is not clear. In studying this issue, we found very little requirement for RhoA-MyoII during cone cell intercalation. Instead, our results indicate a preeminent role for the conserved Notch signaling pathways, adhesion through both Hbs and Rst, and endocytosis. Altogether our results suggest that preferential adhesion between cells is a principal mechanism of slow intercalation.

RESULTS

Adherens junction dynamics during cone cell intercalation

Cone cell intercalation unfolds over 10hrs (Figure 1A-C and Movie S1) and consists of the elimination of the AJ between the anterior and posterior (A/P) cells, followed by the creation of a new AJ between the polar and equatorial (PI/Eq) cells (Figure 1B-C). To establish the cellular dynamics associated with this step of slow intercalation, we used the *Ecad::GFP* transgene to monitor how the AJs evolve as the ommatidium develops. We found that as the cone cells undergo neighbor exchange, they also increase their apical area (Figure 1D-E, Movie S1). Quantification revealed that despite the elimination of the AJ between the A/P cells, the cone cell cluster elongates along the PI/Eq axis upon intercalation (Figure 1F-G). Following this, the cone cell quartet widens along the A/P axis, as the AJ is created between the PI/Eq cells. Further, examining the dynamics of growth of the AJs shared by the four cone cells, we found a cross-correlation between the shrinkage of the A/P cone cell AJ and the expansion of the remaining adjoining AJs (Figure 1H). Thus, a mechanism might

exist whereby membrane removed from the shrinking AJ is recycled to the neighboring AJs. This correlation did not hold when considering the AJs the cone cells share with the primary pigment cells (Figure 1I) suggesting local membrane redistribution between the AJs shared by the cone cells, but not with those shared with the primary pigment cells.

Next, we considered that the primary pigment cells that surround the cone cells could influence cone cell intercalation and shape. These two pigment cells share AJs that run parallel to the PI/Eq axis of the lens and thus, that are aligned with the shrinking cone cell AJ (Figure 1A). As the cone cell AJ shrinks, the AJs shared by the primary pigment cells lengthen (Figure 1C-D), as demonstrated by the negative correlation of their length (Supplementary Figure 1A). Here, we reasoned that the negative correlation could indicate that these processes are linked. To test this idea, we compared the corresponding patterns of AJ length fluctuation by cross-correlating the fluctuation of the lengths of these AJs. However, quantification of this parameter showed that they were not correlated, suggesting that length changes in the primary pigment cell AJs do not directly influence changes in length of the cone cell AJ (Supplementary Figure 1B).

Limited MyoII accumulation at the shrinking adherens junction suggests a minimal role in intercalation.

To assess whether MyoII powers AJ remodeling to induce cone cell intercalation, we analyzed its distribution and intensity over time using a fly strain where the Myosin light chain is tagged with GFP (Sqh::GFP) (Figure 2A-C). We could detect a marginal 10% MyoII enrichment at the shrinking AJ between the A/P cone cells (Figure 2D). This is small when compared to the values of 30-300% enrichment reported for shrinking AJs in the germband (Collinet et al., 2015; Pare et al., 2014; Simoes Sde et al., 2010). Using live imaging, we could also visualize pulsatile apical-medial meshworks of MyoII in the cone cells, but unlike in the intercalating

cells in the germband, we could not detect any flow dynamics toward the shrinking AJ (Figure 2E), nor later on towards the new AJ as it is created between the PI/Eq cone cells (Figure 2F). Altogether, these results suggest that slow cell intercalation in the eye lens is not primarily driven by MyoII contractility.

Modeling cone cell intercalation predicts a predominant role for adhesion.

The small increased Sqh::GFP accumulation at the A/P AJ compared to the adjoining AJs could regulate shrinkage of this AJ, however the small magnitude could mean that this MyoII activity is not sufficient to drive AJ shrinkage, and that instead adhesion between cells might dominate this process. It is also possible that extrinsic regulations are involved, for example from the primary pigment cells that surround the cone cells. To distinguish between these possibilities and assess a potential role for the primary pigment cells during cone cell intercalation, we built a computational vertex model (Farhadifar et al., 2007) of the ommatidium allowing us to vary the relative levels of contractility and adhesion at the cells' AJs.

Vertex models depend on modelling tension at each junction which is a combination of contractility from MyoII and counteracting adhesion forces. Therefore, to set up the vertex model, we quantified the intensity of MyoII at all AJs, and surveyed the principal adhesion molecules that have been shown to be involved in mediating intercellular adhesion in the lens. This includes Ecadherin and Ncad, as well as Rst and Hbs (Bao and Cagan, 2005; Carthew, 2005; Chan et al., 2017) (Figure 3A). Intensity values for each of these adhesion molecules were normalized and summed to give a pan-adhesion parameter, relative to the expression levels on the non-shrinking cone cell AJs (Supplementary table 1). As expression level of MyoII and adhesion may not directly reflect their contribution to junctional tension (e.g. the existence of MyoII on a junction doesn't necessarily mean it is contracting that junction), we used the model to explore the relative weighting (w) that MyoII (w_{myo}) and adhesion (w_{ad}) contribute to junction tension. We then calculated tension values

based on these weighted averages of MyoII and adhesion contributions at the AJs, with MyoII being directly proportional and adhesion inversely proportional to the effective tension of an AJ (see Computational Modelling, Methods, for detailed formula). The adhesion parameter was calculated as the sum of relative intensities of Ecad, Ncad, Hbs and Rst (relative to the cone cell side AJs). This approach allowed us to integrate all these adhesion molecules in the model while accounting for the fact that not all AJs in the ommatidium contain Hbs, Rst and/or Ncad.

Where possible, the tension values were estimated experimentally from laser ablation experiments. Ecad::GFP, Rst::GFP, Hbs::GFP, Sqh::GFP and Ncad staining intensity measurements were quantified for ommatidia in a post-intercalated state (30%APF) (Figure 3A-A''', Movie S2 and S3), and normalized to the average of the non-shrinking cone cell AJs. To set up the model, we applied these tension values to simulated ommatidial cell clusters with post-intercalation topologies (Figure 3C).

We then used the model to explore how cone cell arrangement is affected when varying adhesion and/or contractility through modeling. The tension ranges were obtained by varying the averaging weight by 0, 30, 50, 70 or 100 percent to reflect the varying ratio of contribution of adhesion (cyan) and MyoII contractility (magenta) to tension at the AJ (Figure 3D, y-axis). In addition to varying the tension at the AJs, we simulated a range of cytosolic MyoII contractility levels in the primary pigment cells, whereby contractility in these cells applies tensile forces on the cone cell cluster (Blackie et al., 2020) (Figure 3C, dashed lines; Figure 3D, x-axis). Considering an ommatidium in a stable post-intercalation topology (green zone in Figure 3D heatmap, Figure 3E''), a reduction in AJ adhesion (moving down Y-axis) causes the topology to switch out of post-intercalation topology to the four-way vertex (yellow zone, Figure 3D,E') and even back to the pre-intercalation topology (red zone, Figure 3D,E). Whereas a reduction in cone cell AJ MyoII contractility (moving up Y-axis) coupled with a reduction in primary pigment cell cytoplasmic MyoII (moving left on X-axis), ommatidium can remain in the stable post-intercalation state

even for a significant amount of MyoII reduction (diagonal green zone, Figure 3D). Thus, while a wide range of contractility/adhesion can support stable cone cell intercalation, our model suggests it can be achieved through adhesion, with minimal input from MyoII. Our model also suggests that stable cone cell intercalation might be mechanically influenced by the primary pigment cells (Figure 3D).

A limited role for actomyosin contractility during cone cell intercalation

Our vertex model suggests that there are a range of values of MyoII, adhesion and PPC contractility where intercalation is achieved (green stable zone, Figure 3D). These range from adhesion dominating with little role for MyoII-dependent contractility (upper left region, Figure 3D), to MyoII dominating but only with strong contractile forces from the PPCs to stabilize intercalation (lower right region, Figure 3D). To test which of these is true for the retina, we manipulated MyoII and made predictions from our model for how the tissue would behave for each region. For example, the model predicts tension in the primary pigment cells could help to stabilize intercalation if MyoII dominates cone cell junction tension, therefore perturbing MyoII would have a strong effect on intercalation. If, however, adhesion dominates cone cell intercalation, perturbing primary pigment cell tension would have only minor effects on cone cell intercalation.

To test these suggestions, we perturbed MyoII expression and activity specifically in the cone cells. A prediction from our model is that a reduction in MyoII levels in the cone cells should not push the cone cells back into a pre-intercalation state (Figure 3D – a shift up the y axis stays in the ‘green’ post-intercalation zone). Consistent with this, we found that expression of the dominant negative version of the MyoII heavy chain, Zipper^{DN}::YFP (Barros et al., 2003) had a minimal impact on cone cell intercalation, with less than 5% of the ommatidia examined showing a failure to shrink the A/P AJ (Figure 4A-B). Similarly, expressing a shRNAi (IR) against the heavy chain of MyoII (Zipper; *zip*) in the cone cells interfered with

intercalation in less than 10% of the cases (Figure 4C). In these experiments, we cannot measure how much MyoII activity is inhibited and it is therefore possible we are underestimating the role of MyoII in cone cell intercalation. For this reason and to further probe the contractile actomyosin cytoskeleton, we also examined requirement for the MyoII activator RhoA. Expressing a dominant negative RhoA transgene (RhoA^{N19}) or shRNAi targeting this small GTPase in cone cells, led to significant relaxation of these cells, which strongly suggests inhibition of the contractile actomyosin cytoskeleton (Figure 4D-E). However, this did not affect cone cell intercalation. Therefore, taken together, our experiments indicate a minimal requirement for the contractile actomyosin cytoskeleton during cone cell intercalation.

Next, to assess the second prediction of our vertex model, that if MyoII contractility dominates at the cone cell AJs, then stable intercalation would require pulling tension from the primary pigment cells, we expressed the shRNAi against RhoA specifically in the primary pigment cells (Figure 4F). We found this did not block cone cell intercalation. However, quantification of the length of the AJ that forms between the polar and equatorial cone cells after intercalation showed that this AJ was shorter (Figure 4F',F''). Specific expression of the shRNAi transgene was controlled by expressing a UAS-RFP protein (Supplementary figure 2). Thus, while regulation of the contractile actomyosin cytoskeleton in the pigment cells promotes lengthening of the AJ between the Equatorial and polar cone cells, stable intercalation is still achieved, which, put together with the predictive heatmap generated by our model (Figure 3D), suggests that this tissue lies towards the upper/left stable region where intercalation is mainly adhesion dominated.

Rst and Hbs regulate cone cell intercalation.

A likely process that might induce cone cell intercalation is intercellular adhesion. Amongst the adhesion molecules that might play a role in these cells are Rst and Hbs. In the case of the cone cells, and with analogy to how these two factors promote preferential adhesion between interommatidial cells (Bao and Cagan, 2005, Bao et al, 2010), we reasoned that one cone cell expressing Hbs would favor adhesion with one expressing Rst. This type of interaction in *trans* could stabilize the newly created AJ between the PI and Eq cone cells. To test this hypothesis, we first examined the pattern of Rst and Hbs expression in the cone cells through time. Use of endogenously tagged Rst::GFP and Hbs::GFP showed that both these adhesion molecules are localized at the AJs the cone cells share with the surrounding primary pigment cells. However, we could not detect these GFP fusions at the AJs between the cone cells (Figure 5A-F). Enrichment for Rst::GFP and Hbs::GFP was higher on the AJs between primary pigments cells and the A/P cone cells than with the Eq/PI cone cells (Figure 5A''',3A'''). In addition, both Hbs::GFP and Rst::GFP were enriched at the AJs shared by the primary pigment cells, and at the AJs shared between the primary pigment cells and the interommatidial cells as previously reported (Figure 5A-F). While these experiments do not allow us to establish in which cell Hbs and Rst are expressed (ie on which side of the AJ), they are compatible with a Rst-Hbs interface taking place between the cone and the primary pigment cells (Figure 5G).

To examine this possibility, we used shRNAi to decrease the expression of *hbs*. When expressed in either the Eq and PI cells, this led to limited defects in intercalation with a minority (ie 10 to 15%) of clusters failing to elongate the new AJ to complete intercalation (Figure 5H' and Figure 5I). Decreasing *hbs* expression in the A and P cone cells led to a worse phenotype, where up to 30% of the clusters fail

to shrink the A/P cone cell AJ (Figure 5H'' and Figure 5I). In addition, it also led to other defects in cone cell configuration, whereby the mutant cell rounded up to minimize its interface with the flanking primary pigment cell (Figure 5H''' and Figure 5I). Altogether, these results confirm previous work (Grillo-Hill and Wolff, 2009). Interestingly, decreasing the expression of *hbs* in all four cone cells had very little effect on their intercalation, suggesting differential Hbs expression amongst these four cells is required. These results and the pattern of Hbs expression suggest that interaction between the cone and primary pigment cells are at play in cone cell intercalation.

To determine whether Rst is also required, we made use of the *rst*⁶ mutant allele. Homozygous *rst*⁶ animals are viable, and as noted before (Grillo-Hill and Wolff, 2009), cone cell intercalation occurs normally in these animals. Based on our results that no defects in intercalation are observed when all cone cells are deficient for Hbs, we reasoned that a role for Rst might only be revealed in mosaic situations, when some cone cells are wild type. To test this idea, we recombined the *rst*⁶ allele onto an FRT chromosome and generated somatic mutant clones. This approach showed that removing *rst* specifically in the PI and Eq cone cells leads to defects in intercalation (Figure 5J-J', quantified in Figure 5K). In these experiments, up to 40% of the ommatidia presenting both PI and Eq *rst*⁶ mutant cone cells failed to intercalate properly. In addition, a small proportion (less than 10%) of the clusters containing an A or P cone cell mutant for *rst*⁶, also show defects in intercalation. Altogether, the requirement we find for *hbs* and *rst* in the cone cells using mosaic analysis suggest that differential Hbs/Rst activity is required for cone cell intercalation.

Cone cell intercalation is regulated by the primary pigment cells.

A and P cone cells deficient for *hbs* expression minimize their AJ with the surrounding pigment cells suggesting a model whereby adhesion between these cells and the surrounding primary pigment cells could be regulated by the Hbs-Rst

system. In this hypothesis, Rst would be required in the primary pigment cells. To test this, we examined ommatidia lacking *rst* in one or both primary pigment cells. Firstly, we could confirm that decreasing *hbs* expression in the primary pigment cells did not affect cone cell intercalation (Grillo-Hill and Wolff, 2009) (Figure 5L). In contrast, we found that abolishing *rst* expression in both primary pigment cells, affected cone cell intercalation in ~65% of the cases (Figure 5M). In addition, 35% of the cases had cone cell configurations resembling those seen when decreasing the expression of *hbs* in the A and P cone cells (Figure 5H'''). Together with the patterns of Rst::GFP and Hbs::GFP expression (Figure 5G), these results support the model that the interface between the A and P cone cells and the surrounding pigment cells is promoted by the Hbs-Rst adhesion system, with Hbs in the cone cells engaging in *trans* with Rst expressed in the surrounding primary pigment cells.

Notch signaling regulates cone cell intercalation.

Previous studies have shown that the expression of Hbs in the primary pigment cells is regulated by Notch (Bao, 2014). This connection and the finding that Hbs regulates cone cell intercalation prompted us to investigate the role of Notch in this process. Firstly, we examined the distribution patterns of Notch and its ligand Delta before and after intercalation using live imaging of functional GFP-tagged proteins (Figure 6A-B) (Corson et al., 2017; Trylinski et al., 2017). At the onset of cone cell intercalation, we found that Notch was present at the apical cortex of all cone cells (Figure 6A) whereas, confirming previous observations (Bao, 2014), we found that DI was highly expressed in the A cell and to a lesser extent, in the P cell (Figure 6B). We also examined the distribution of Neuralized (Neur), a developmentally regulated E3 ubiquitin ligase that is required for DI endocytosis and N receptor activation (Figure 6C) (Schweisguth, 2004; Weinmaster and Fischer, 2011). While Neur was detected in all cone cells, we observed a higher level in the A and P cells. These patterns of expression suggest that high levels of DI in the A cell activate N in the P,

PI and Eq cell. To test this suggestion, we monitored N signaling over time by measuring activated nuclear Notch, or NICD, in the cone cells of living NiGFP pupae (endogenous Notch was tagged with GFP in its intracellular domain so that nuclear GFP reveals NICD; Figure 6D and 6E) (Couturier et al., 2012). NICD was detected in the PI and Eq cells before and after intercalation. In contrast, NICD was detected in the P cell only before intercalation, suggesting that loss of direct contact with the A cell results in loss of N receptor activation. Finally, NICD was not detected in the A cell, further suggesting that this cell is the DI signal-sending cell within the cone cell quartet. This pattern of N activity was confirmed by examining the expression of two direct N targets, *E(spl)m δ -HLH* (Figure 6F) and *E(spl)m3-HLH* (not shown) using GFP-tagged proteins. Altogether, our analysis revealed that directional signaling occurs within the cone cell quartet and that a specific change in the pattern of N activity correlates with cone cell intercalation.

To test whether N signaling contributes to cone cell intercalation, we used a dominant-negative version of Mastermind, Mam^{DN}, that blocks transcription downstream of N (Giraldez et al., 2002). Expressing Mam^{DN} in all four cone cells led to defects in their intercalation (Figure 6G-H). Live imaging of these retinas revealed that these defects were due to failures in stabilizing the new PI/Eq AJ, which led to reversion to the original configuration with an AJ between the A and P cells (Movie S4 and Figure 6I). In good agreement with our finding that N is active in the Eq and PI cells throughout intercalation, examination of ommatidia mosaic for *Mam^{DN}* revealed a strong requirement for transcriptional regulation downstream of N in each of these two cells (Figure 6J-K). From these experiments, we conclude that signaling from either the A or P cell is sufficient to activate N in the Eq and PI cells and that N activity in the Eq and PI cone cells is critical for intercalation. This pattern of N and the requirement for Hbs in all cone cells does not suggest a simple Notch-Hbs link in

this case. In addition, expressing Hbs in PI/Eq cone cells also expressing Mam^{DN}, did not rescue the intercalation phenotype (not shown).

Endocytosis is required at all stages of cone cell intercalation.

Our finding suggesting that membrane is recycled from the shrinking junction to the neighboring junctions (Figure 1H) led us to hypothesize that endocytosis is involved in intercalation by promoting membrane removal during AJ shrinkage. To test this idea, we used the thermo-sensitive Shibire^{ts1} protein (ortholog of *dynamain*). Inhibiting endocytosis in the cone cells as they intercalate caused the AJs they share to become convoluted (Figure 7A). We therefore conclude that endocytosis regulates membrane turnover during cone cell intercalation. Additionally, cone cell intercalation was blocked either during AJ shrinkage (72% of cases) or at the four-way vertex (18% of cases) (Figure 7B-C) when assayed at a stage where in wild-type retinas roughly 100% of the ommatidia should have completed intercalation.

In order to refine this analysis, we then inhibited endocytosis for only 4hrs during each of the three stages of cone cell intercalation: AJ shrinkage, four-way vertex and AJ elongation (Figure 7D-F). In these experiments, intercalation was stalled or reverted to an earlier stage in a significant number of cases (Figure 7G). Time-lapse imaging confirmed that inhibition of endocytosis caused a failure in cone cell A/P AJ shrinkage (Movie S5). In agreement with our quantifications (Figure 7G), live imaging revealed that inhibiting endocytosis at the four-way vertex stage (24%APF) led to reversions to the initial cone cell configuration (Figure 7H). Altogether these results demonstrate that endocytosis is required for stable intercalation to proceed between the cone cells. AJ convolution is compatible with an excess of plasma membrane, which is consistent with a role for endocytosis in shedding membrane during slow intercalation.

Another aspect of cone cell intercalation that is expected to be affected when blocking endocytosis, is the N pathway, as N-signaling requires endocytosis of DI. To test this, we specifically targeted DI endocytosis by over-expressing a stabilized version of Bearded (Brd) (Leviton et al., 1997), called Brd^R (Perez-Mockus et al., 2017). We found that expression of Brd^R simultaneously in the A and P cone cells led to defects in intercalation in 40% of the cases, while expressing Brd^R in either the A or P cell rarely led to defective intercalation (Figure 7I). Thus, next to promoting membrane removal, endocytosis is also required for N-activity in cone cell intercalation.

DISCUSSION

Most instances of epithelial cell intercalation studied so far have focused on rapid neighbor exchanges, occurring over periods of tens of minutes, as is the case in the fly germband (Bertet et al., 2004; Zallen and Wieschaus, 2004), or a couple hours as during kidney tubule morphogenesis and early retinal development (Lienkamp et al., 2012 ; Robertson et al., 2012). Intercalation of the cone cells in the fly is much slower as it unfolds over ~10 hours. Combining mathematical modeling and genetics experiments, we found that it involves regulations that appear more complex than the ones found to control faster intercalation (Heisenberg and Bellaiche, 2013; LeGoff and Lecuit, 2015). Our results show that cone cell intercalation requires transcription downstream of Notch in two of the four intercalating cells. We also find that cone cell intercalation shows a low requirement for the contractile MyoII pathways, and instead, relies more on adhesion, regulated by Rst and Hbs. In addition, our experiments suggest that membrane endocytosis is essential for stable intercalation by shedding plasma membrane during AJ shrinkage and by promoting N-activation. Finally, we present evidence that cone cell intercalation involves processes extrinsic to the cone cell quartet, involving tensile force and adhesion in the neighboring cells.

The RhoA-MyoII axis is largely dispensable for cone cell intercalation

We found a small enrichment for MyoII at the shrinking cone cell AJ, suggesting that it could contribute to inducing shrinkage of the AJ over time. In addition, inhibiting the activity and expression of this motor protein led to cone cell intercalation defects in approximately 10% of the ommatidia we examined. Therefore, MyoII plays a limited role during cone cell intercalation. However, we cannot exclude the possibility that residual MyoII levels are present in our genetic perturbations, which are sufficient to promote cone cell intercalation. Our perturbations of RhoA, an upstream regulator of the actomyosin cytoskeleton, show that while RhoA inhibition in cone cells leads to a relaxation of their apical profile, intercalation is not impacted. These experiments also support our model that MyoII is minimally required in cone cell intercalation. This conclusion is also consistent with recent work revealing that normal cone cell intercalation requires Ncad to downregulate MyoII at the AJs shared between the cone cells (Chan et al., 2017). Therefore, irrespective of potential redundancies in MyoII activation in retinal cells, this work and our present study strongly suggest that MyoII concentration/activity needs to be limited at the cone cell AJs for intercalation to proceed normally. This situation is somewhat analogous to that reported in the fly notum where lowering MyoII activity allows for tissue fluidity (i.e. neighbor exchange) (Curran et al., 2017). However, unlike in the notum, AJ remodeling is not stochastic but deterministic in the cone cells.

Adhesion regulates cone cell intercalation.

We found that both Hbs and Rst regulate cone cell intercalation. However, the general adhesion logic at play between the cone cells, and also between them and the surrounding primary pigment cells is not clear. Hbs is required in all individual cone cells, and our work argues that it plays a role in stabilizing the new AJ created between the Eq and PI cells after intercalation. Rst in the Eq/PI cells also contributes to regulating creation of this AJ. It is therefore possible that a Hbs/Rst interaction in

trans takes place between the Eq/PI cells to stabilize the newly created AJ. However, Rst::GFP and Hbs::GFP show no detectable enrichment at these AJs. In fact, one of the strongest effects on cone cell intercalation is seen when *rst* is removed from the primary pigment cells. Rst::GFP and Hbs::GFP are detected at the AJ between these cells and the cone cells. We therefore hypothesize that Hbs-Rst interactions take place between these two cell types. In this hypothesis, we envisage that Hbs expressed in the cone cells contacts Rst expressed in the primary pigment cells. The primary pigment cells also express Hbs, which accumulates at the AJ they share with the interommatidial cells (Bao and Cagan, 2005). Our work therefore raises the possibility that the primary pigment cells express both Rst and Hbs, and that these proteins have a planar polarized distribution in this cell type. This possibility is consistent with our finding that both Rst and Hbs are strongly localised to the AJ between the two primary pigment cells.

Notch-signaling between cone cells regulates intercalation.

In addition to a role for Hbs and Rst, our work also revealed that a N-DI code exists between the four cone cells that regulates their intercalation. In this code, DI signals from the A or P cell whereas N is activated and required in the Eq and PI cells. This function for N requires transcription since it is blocked by Mam^{DN}. Previous work has established that N can induce Hbs expression (Bao, 2014). However, the pattern of N activation in the Eq/PI cells and the requirement for Hbs in all cone cells does not suggest a Notch-Hbs pathway in this case. Thus, more work will be required to understand how N regulates intercalation and how expression of Hbs and Rst is controlled in the cone cells. We also note that Notch activation has previously been placed downstream of the Hbs-Rst system in the eye (Singh and Mlodzik, 2012). Such regulation could also be at play during cone cell intercalation. Considering N signaling between the cone cells, it is possible that perturbing Hbs/Rst expression in these cells might affect the DI-N interface by changing the surface contact these cells share.

Endocytosis and cone cell intercalation

Our work reveals a key function for membrane endocytosis during cone cell intercalation. This could be due to several reasons. Blocking endocytosis in the primary pigment cells leads to defects in Rst localization (Johnson et al., 2008), and by analogy, blocking endocytosis in the cone cells could also affect the Rst/Hbs pathway and thus intercalation. Similarly, endocytosis of DI is required to activate the Notch pathway (Schweisguth, 2004; Weinmaster and Fischer, 2011). Indeed, blocking DI endocytosis by expressing *brd*^{DN} in the A/P cone cells interferes with intercalation. Endocytosis is also likely to be required to control the turnover of Ecad/Ncad in the cone cells and promote plasma membrane removal during AJ shrinkage. For instance, as these cells intercalate Ecad becomes depleted from the AJ between the cone cells and Ecad overexpression in the Eq/PI cone cells blocks intercalation (Carthew, 2005). It is possible that endocytosis promotes this inhibition. Consistent with this type of model, similar regulation of Ecad endocytosis takes place in the fly embryo during intercalation to shrink AJs (Levayer et al., 2011).

Extrinsic regulation of cone cell intercalation.

In addition to showing a dominant role for adhesion over MyoII in regulating cone cell intercalation, our vertex model also predicts that external tensile forces in the surrounding primary pigment cells could play a role (Fig. 3D, moving left on X-axis in the heat map). The primary pigment cells present medial meshworks of actomyosin that are contractile (Blackie et al., 2020). This contractility regulates the width of these cells' apical profiles and would be expected to pull onto the AJ these cells share with the A and P cone cell. Perturbing the actomyosin cytoskeleton in the primary pigment cells by inhibiting *RhoA* expression led to a decrease in the length of the cone cell central contact but did not completely block intercalation (Fig. 4E-F). Taken together with the fact that reduction of MyoII in the cone cells doesn't inhibit

intercalation but reduction of adhesion does, this suggests that ommatidia lie in the upper/left section of the predictive heatmap generated by our model, whereby this slow mode of intercalation is dominantly driven by adhesion within the cone cells.

MATERIALS AND METHODS

Fly strains

Flies were raised on standard food at 18°C. Crosses were performed at 25°C or 29°C as stated. The following fly strains were used:

;Ecad::GFP; (Huang et al., 2009).

sqh^{AX3}; sqh>sqh::GFP; (BL #57144, (Royou et al., 2002)).

;Sp/CyO;pros-Gal4/TM6 (Gift from T. Cook).

;GMR-Gal4; (Freeman, 1996).

;;UAS-shibire^{ts1} (BL #44222, (Koenig and Ikeda, 1983)).

;UAS-YFP-MyoII^{DN}; (Barros et al., 2003).

rst⁶;; (Wolff and Ready, 1991)

ubiGFP,FRT19A;eyFlp.

;eyFlp;FRT40,GMR-myrRFP/CyO;

rst::GFP;; (BL #59410).

;hbs::GFP; (BL #65321).

;UAS-hbsRNAi; (VDRC #105913, VDRC #40896).

;UAS-rstRNAi; (VDRC #951, VDRC #27223).

hsflp;;act>CD2>GAL4,UAS-RFP (BL #30558).

hs-flp;actin>y>gal4,UAS-mCherry;armGFP/TM6.

;;UAS-Mam^{DN} (BL #26672, (Helms et al., 1999).

Neur::GFP, a BAC transgenic line with two copies of GFP-tagged Neur (Perez-Mockus et al., 2017).

ubi-Baz::mCherry (Bosveld et al., 2012);

UAS-Brd^f (Perez-Mockus et al., 2017).

Di::GFP, a GFP knock-in allele (Corson et al., 2017).

Ni::GFP, a GFP knock-in allele (Trylinski et al., 2017).

E(spl)m3-HLH::GFP, a GFP knock-in line (Couturier et al., 2019)

E(spl)m δ -HLH::GFP, a BAC transgenic line expressing GFP-tagged *E(spl)m δ -HLH* (Couturier et al., 2019).

w;;FRT82B, ubi-nlsRFP (BL-30555)

UAS-shRNAi RhoA, (BL-27727)

;SpaGal4;ProsGal80

w; UAS-RhoA^{N19} (BL-7328)

Transgenes

The *prospero* eye enhancer (Charlton-Perkins et al, 2017) was PCR-amplified from the *prosGal4* plasmid (gift from Tiffany Cook) and CACC added to the 5' end using the following primers: 5' CACCATCTGTGACGAAGACACTCGTTTTGAG 3' and 5' TCGATTGCCAGGAAGTGCAGG 3'. PCR fragment was cloned into *pENTRTM/D-TOPO* vector (Invitrogen) and then sequence-verified. The Gateway Cloning System (Invitrogen) was used to insert the *pros* enhancer into the *pBPGal80Uw-6* destination vector (Addgene) to generate *prosGal80* plasmid. Transgenic flies were generated using standard procedures (Bestgene) and *prosGal80* was inserted into attP2.

Clonal analysis

To generate mosaic ommatidia, *hs-flp;;actin>CD2>gal4,UAS-RFP* or *hs-flp;actin>y+>gal4,UAS-mCherry;arm-GFP/TM6* were crossed to *UAS-* transgenes of interest. Flies were heat shocked at third instar larval stage at 37°C for 10-15 mins and then dissected 2-3 days later at 40%APF (25°C). To generate *rst^f* mosaics, the *rst^f* was recombined onto an FRT19A chromosome, which was then used in

combination with an FRT19A, ubi-GFP; eyFLP strain. The Coin-FLP system (Bosch et al., 2015) was used to generate mosaics expressing shRNAi targeting RhoA. Animals were raised at 18°C.

Inhibition of endocytosis using *shibire*^{ts1}

UAS-shibire^{ts1} flies were crossed to *prosGal4* flies and raised at 25°C until the stated time of development, then transferred to 31°C to block endocytosis for either 4hrs or overnight. Retinas were dissected at 40% APF and scored for progression of cone cell intercalation.

Antibodies and immunostaining

Pupae were staged at 25°C or 29°C to 40%APF then retinas were dissected in PBS on ice and fixed in 4% paraformaldehyde for 20mins at room temperature (RT). Retinas were washed in PBS-Triton 0.3% (PBS-T) then stained with primary antibody in PBS-T for 2hrs at RT or overnight at 4°C. Retinas were washed in PBS-T and then stained with secondary antibodies for 2hrs at RT. Retinas were mounted in Vectashield (Vectorlabs). The following antibodies were used: mouse N2 A71 anti-Armadillo (1:50), deposited to the DSHB by Wieschaus, E. (DSHB Hybridoma Product N2 7A1 Armadillo) (Peifer and Wieschaus, 1990), DCAD2 anti-E-Cadherin (1:50), deposited to the DSHB by Uemura, T. (DSHB Hybridoma Product DCAD2) (Yoshida-Noro et al., 1984) DN-Ex anti-N-Cadherin (1:50), deposited to the DSHB by Uemura, T. (DSHB Hybridoma Product DN-Ex) (Iwai et al., 1997) combined with mouse or rat secondary antibodies conjugated to Dy405, Alexa488, Cy3 or Alexa647 (Jackson ImmunoResearch) as appropriate, used at 1:200. Images of fixed retinae were acquired on a Leica SPE, Leica SP5 or Leica TCS SP8 confocal microscope. A 40x oil objective was used for imaging of whole retinas for quantification and a 63x oil objective was used for higher magnification images.

Image processing

All images presented were processed using FIJI (Schindelin et al., 2012) and AdobePhotoshop CS4 (Adobe). Graphs were produced in Excel (Microsoft), GraphPadPrism 7 (GraphPad) or MATLAB R2017a (Mathworks). Figures were mounted in Adobe Illustrator CS4 (Adobe).

Statistical tests

Statistical tests were performed in GraphPad Prism 7. Data was compared using a T-test (paired or unpaired as appropriate) or One-way ANOVA with Tukey's post-hoc tests.

Time-lapse imaging

Ecad::GFP, *Ecad::GFP/Ecad::GFP;UAS-Mam^{DN}/pros-Gal4* or *Ecad::GFP/+;UAS-shibire^{ts1}/pros-Gal4* flies were staged to between 10-20%APF at 25°C and the pupal case removed at the dorsal end to expose the retina. Pupae were mounted on blue-tac with the retina facing upwards and covered with a coverslip as previously described (Fichelson et al., 2012) and (Couturier et al., 2014). Time-lapse imaging was performed on a Zeiss inverted microscope with an Andor spinning disc using a Plan Neofluar 100x/1.3 Ph3 oil immersion objective. Images were acquired using ImageJ Micromanager software (Edelstein et al., 2010) . Retinas were imaged for a minimum of 12hrs taking a Z-series in 1µm sections every 5mins. Drift in XY and Z was corrected manually. Images were post processed in FIJI to further correct for drift. For *Ecad::GFP; UAS-shibire^{ts1}/pros-Gal4*, flies were raised at 25°C until 15-20% APF and then transferred to the microscope and incubated at 31°C to stimulate endocytosis inhibition as soon as imaging began. Nuclear N levels were measured over time in *NiGFP* pupae using small z-stacks centered at the nucleus level. Image acquisitions were performed at 20 ± 2°C, using a laser scanning confocal microscope (LSM780; Zeiss) with a 63x (Plan APO, N.A. 1.4 DIC M27) objective.

Laser ablation

Ecad::GFP pupae were raised and mounted as for time-lapse imaging experiments. Ablations of AJ between primary pigment cells and between interommatidial cells, were performed using a Zeiss LSM880 microscope with a Plan Apochromat 63x/NA1.4 oil objective using 740nm multiphoton excitation from a Ti-sapphire laser. An ROI of 3x3 pixels was drawn over an *AJ* and ablated with 5-10% laser power at the slowest scan speed for 1 iteration. Images were acquired every 1sec after ablation. Settings were optimized by imaging *sqh^{Ax3};sqh::GFP*; flies during ablation to ensure only the AJ-associated MyoII was removed and that the medial meshwork of MyoII remained intact. The AJs repaired after every instance of ablation, indicating that the cell was not damaged. Positions of the two adjoining vertices after ablation were manually tracked using FIJI and the distance between them calculated at each frame after ablation. Recoil velocity was calculated by a linear fit across the first frames after ablation. One-way ANOVA was performed in GraphPad Prism7 to compare stages.

Cone cell area through time

The Tissue Analyser FIJI plugin (Aigouy et al., 2010) with manual correction was used to segment the cone cells on a time-lapse (5mins/frame) of *;Ecad::GFP*; retinas. The areas of individual cone cells were then measured and averaged across four ommatidia.

Cone cell axes length through time

The perimeter of the cone cell cluster was traced manually using the Freehand selection tool in FIJI on every 20th frame (100mins) of time-lapse of *;Ecad::GFP*; retinas. To measure A/P and Eq/PI axes length an ellipse was fitted over the cone cells, measured over time and then expressed as a ratio. Measurements were

averaged for each time point over 13 time-registered ommatidia from two independent retinas.

AJ perimeter measurements

AJ lengths were taken as the inter-vertex distance and were measured manually on each frame of time-lapse movies of ;*Ecad::GFP*; retinas using the line tool in FIJI. Measurements were averaged from 13 time-registered ommatidia from two independent retinas.

Cross-correlation of AJ length

Curves of AJ length over time for the cone cells were smoothed by taking a five-point moving average. Data were detrended by taking the running difference to find the change in AJ length over time. Cross-correlation was performed in R statistical package using the ccf function. The mean cross-correlation function was calculated as the average correlation coefficient at each time lag across 13 ommatidia from two independent retinas.

Intensity at the AJs

sqh^{AX3};sqh-sqh::GFP; / rst::GFP;; / ;hbs::GFP; / EcadGFP or CantonS flies stained for Ncad were staged to 30% APF and retinas were dissected, fixed and stained against Arm. Retinas were imaged on a confocal microscope (Leica SP5) using the same settings for each retina. A Z-projection was generated over the depth of the AJs in FIJI. A 7 pixel wide line was drawn over each AJ in the Arm channel and the intensity of each channel was averaged over this line, except for the cone-primary pigment cell AJs, as the *Sqh::GFP* was found to be present only on one side of the AJ, a 4 pixel (~ half of 7) line was drawn over the *Sqh::GFP* channel. To control for variations in staining and/or imaging, all individual values within each image were normalized by dividing by the average value for the adjoining cone cell-cone cell AJs for that image. One-way ANOVA followed by Tukey's post hoc tests for pairwise

comparison was performed using GraphPad Prism 7. For comparison of cone cell-cone cell AJs, a paired T-test was performed paired by ommatidia.

Scoring cone cell intercalation

Retinas were dissected at 40% APF, fixed and stained for Arm to label the AJs. Whole retinas were imaged with a 40x objective taking a Z-series in 0.5µm slices in two tiles. Tiles were manually aligned and combined using Align3 TP plugin in FIJI. Ommatidia were manually scored for stage of cone cell intercalation across each retina. Stage was determined by comparing the position of the central cone cell-cone cell AJ and the two AJs shared by the primary pigment cells (parallel = AJ shrinkage stage and perpendicular = AJ elongation stage). Percentages were calculated for each retina and then the average percentages and standard deviations were calculated for each genotype. For large clones, ommatidia were compared from inside and outside the clones. For single cell clones, relative position of cells (A, P, Eq and Pl) was recorded and ommatidia were grouped into categories by which cells were affected.

Scoring switches between stages of cone cell intercalation

For the *Ecad::GFP*; and *;Ecad::GFP/Ecad::GFP;UAS-Mam^{DN}/pros-Gal4* time-lapse movies, ommatidia were scored for which stage of cone cell intercalation they were in for each frame of the movie (5min intervals). A 'switch' in a given frame is defined as being scored as at a different stage to that of the previous frame. The total number of switches was measured from 10% of retinal development (before cone cell intercalation) for roughly 12hrs (until after cone cell intercalation is completed in the wild type).

Particle Image Velocimetry (PIV)

sqh^{AX3};sqh-sqh::GFP; ommatidia were imaged on a Zeiss LSM880 microscope with a Plan Aplanachromat 63x/NA1.4 oil objective using airyscan detectors to increase

resolution. Movies were processed by Bleach correction, Gaussian blur and registered with the Stack-reg plugin (Thevenaz et al., 1998) if needed in FIJI. PIV analysis was performed using the FIJI PIV plugin (Tseng et al., 2012), by choosing an 8x8 pixel window with a time lag 4.34 seconds. Cell contours were tracked using the Tissue Analyzer plugin (Aigouy and Le Bivic, 2016) in FIJI or manually in FIJI to segment the cone cells. The angles of each PIV vector within the cone cells over time were plotted in a polar histogram in MATLAB to show lack of overall directional flow.

Computational modeling

The ommatidium was modelled using the well-established cellular vertex model (Farhadifar et al., 2007). In vertex models, cells are described by the polygons formed of their contacting edges. These edges represent the attached contacting surfaces (membrane and actomyosin cortices) of both cells. The positions of vertices forming all edges are traced, and the energy minimization is carried out over these positions. The energy of the system is defined by the combined energy contributions of: i) cell area conservation, the deviation of each cell from its ideal size, ii) combination of tension and adhesion energies at each contacting cell-cell boundary (1).

$$E(\mathbf{R}_i) = \underbrace{\sum_{\alpha} \frac{K_{\alpha}}{2} (A_{\alpha} - A_{\alpha}^{(0)})^2}_{(i)} + \underbrace{\sum_{i,j} \Lambda_{i,j} l_{i,j}}_{(ii)} \quad (1)$$

Here, $E(\mathbf{R}_i)$ is the total energy of the system for a given set of vertex position (\mathbf{R}_i) that the algorithm minimizes. The system is composed of N_c cells ($a = 1 \dots N_c$), and N_v vertices ($i = 1 \dots N_v$). For area conservation term (i), K_{α} is the elasticity coefficient, A_{α} is the current area of the cell, and $A_{\alpha}^{(0)}$ is the ideal area. For the tensile/adhesive contact energy contribution (ii), Λ_{ij} is the line tension coefficient for the junction couple

(i,j), and l_{ij} is the length of the junction between vertices. For the simulations in this manuscript, the base tension is $\Lambda_{ij}^0 = 0.26$, base $A_{\alpha}^{(0)}$ is 1.0 (see Supplementary Table 1, Figure 3), and K_{α} is 1.0. The small cone cell area is set to $A_{\alpha}^{(0)}$ and remaining cell sizes are scaled accordingly with experimental size scaling measurements (Sup. Table 1). The symmetrical side junctions in between the cone cells are selected as the base, similar to experimental intensity measurements depicted in Figure 3A-A'''. A weighted average of the adhesion and myosin intensity measurements (Figure 3B') are used as surrogate for scaling tension values (Sup Table 1). To scale the tension contribution of adhesion to a cell-cell junction, the base tension level is scaled inversely to normalized adhesion intensity of the junction. For scaling MyoII levels, the tension is scaled directly proportional to normalized MyoII intensity. This is given in the following equation:

$$\Lambda_{ij} = \Lambda_{ij}^0 S$$

$$S = w_{myo} c_{myo} + w_{ad} / c_{ad}$$

$$w_{myo} + w_{ad} = 1$$

Where S is a scaling factor for the line tension, (w) are the averaging weights of myosin and adhesion and (c) are the normalized intensities. During the post-intercalation (late) phase, the primary pigment cell contact and contacts between interommatidial cells on the sides of the ommatidium were not significantly different, whereas the tension on the top & bottom interommatidial cell contacts was 51 percent higher (Figure 3C). The laser ablations depict the true tension of a bond, and model parameters are scaled accordingly where information is available (Sup Table 1). Simulations are carried out on a setup of 91 connected ommatidia with fixed boundaries, and analysis is done on the central ommatidium.

Acknowledgements

We are grateful to Tiffany Cook for providing us with the *prosGal4* line and plasmid, and to the Pichaud lab and Shiladitya Banerjee (UCL IPLS) for discussions related to this study. Stocks obtained from the Bloomington Drosophila Stock Center (NIH P40OD018537) and the Vienna Drosophila Resource Center were used in this study. This work was funded by an MRC (MC_UU_12018/3), BBSRC (BB/R000697) and Royal Society grant (Award #181274) to F. Pichaud, and benefited from MRC core funding to the LMCB, covering access to microscopy (MC_12266B). M. Tozluoglu was funded by a Sir Henry Wellcome Fellowship (Grant No: 103095). Y. Mao is funded by an MRC Fellowship MR/L009056/1, a UCL Excellence Fellowship, a Lister Institute Research Prize Fellowship and EMBO Young Investigator Program. The work of F. Schweisguth's lab is supported by FRM-DEQ20180339219 and ANR-10-LABX-0073 grants. M. Trylinski is supported by an ARC fellowship.

REFERENCES

- Aigouy, B., Farhadifar, R., Staple, D. B., Sagner, A., Roper, J. C., Julicher, F. and Eaton, S.** (2010). Cell flow reorients the axis of planar polarity in the wing epithelium of *Drosophila*. *Cell* **142**, 773-786.
- Aigouy, B. and Le Bivic, A.** (2016). The PCP pathway regulates Baz planar distribution in epithelial cells. *Sci Rep* **6**, 33420.
- Bao, S.** (2014). Notch controls cell adhesion in the *Drosophila* eye. *PLoS Genet* **10**, e1004087.
- Bao, S. and Cagan, R.** (2005). Preferential adhesion mediated by Hibris and Roughest regulates morphogenesis and patterning in the *Drosophila* eye. *Dev Cell* **8**, 925-935.
- Barros, C. S., Phelps, C. B. and Brand, A. H.** (2003). *Drosophila* nonmuscle myosin II promotes the asymmetric segregation of cell fate determinants by cortical exclusion rather than active transport. *Dev Cell* **5**, 829-840.
- Bertet, C., Sulak, L. and Lecuit, T.** (2004). Myosin-dependent junction remodelling controls planar cell intercalation and axis elongation. *Nature* **429**, 667-671.
- Blackie, L., Walther, R. F., Staddon, M. F., Banerjee, S. and Pichaud, F.** (2020). Cell-type-specific mechanical response and myosin dynamics during retinal lens development in *Drosophila*. *Mol Biol Cell* **31**, 1355-1369.
- Blankenship, J. T., Backovic, S. T., Sanny, J. S., Weitz, O. and Zallen, J. A.** (2006). Multicellular rosette formation links planar cell polarity to tissue morphogenesis. *Dev Cell* **11**, 459-470.
- Bosch, J. A., Tran, N. H. and Hariharan, I. K.** (2015). CoinFLP: a system for efficient mosaic screening and for visualizing clonal boundaries in *Drosophila*. *Development* **142**, 597-606.
- Bosveld, F., Bonnet, I., Guirao, B., Tlili, S., Wang, Z., Petitalot, A., Marchand, R., Bardet, P. L., Marcq, P., Graner, F., et al.** (2012). Mechanical control of morphogenesis by Fat/Dachsous/Four-jointed planar cell polarity pathway. *Science* **336**, 724-727.
- Cagan, R.** (2009). Principles of *Drosophila* eye differentiation. *Curr Top Dev Biol* **89**, 115-135.
- Cagan, R. L. and Ready, D. F.** (1989). The emergence of order in the *Drosophila* pupal retina. *Dev Biol* **136**, 346-362.
- Carthew, R. W.** (2005). Adhesion proteins and the control of cell shape. *Curr Opin Genet Dev* **15**, 358-363.
- Chan, E. H., Chavadimane Shivakumar, P., Clement, R., Laugier, E. and Lenne, P. F.** (2017). Patterned cortical tension mediated by N-cadherin controls cell geometric order in the *Drosophila* eye. *Elife* **6**.
- Charlton-Perkins, M. A., Sandler, E. D., Buschbeck, E. K. and Cook, T. A.** (2017). Multifunctional glial support by Semper cells in the *Drosophila* retina. *PLoS Genet* **13**, e1006782.
- Collinet, C., Rauzi, M., Lenne, P. F. and Lecuit, T.** (2015). Local and tissue-scale forces drive oriented junction growth during tissue extension. *Nat Cell Biol* **17**, 1247-1258.

- Corson, F., Couturier, L., Rouault, H., Mazouni, K. and Schweisguth, F.** (2017). Self-organized Notch dynamics generate stereotyped sensory organ patterns in *Drosophila*. *Science* **356**.
- Couturier, L., Mazouni, K., Corson, F. and Schweisguth, F.** (2019). Regulation of Notch output dynamics via specific E(spl)-HLH factors during bristle patterning in *Drosophila*. *Nat Commun* **10**, 3486.
- Couturier, L., Trylinski, M., Mazouni, K., Darnet, L. and Schweisguth, F.** (2014). A fluorescent tagging approach in *Drosophila* reveals late endosomal trafficking of Notch and Sanpodo. *J Cell Biol* **207**, 351-363.
- Couturier, L., Vodovar, N. and Schweisguth, F.** (2012). Endocytosis by Numb breaks Notch symmetry at cytokinesis. *Nat Cell Biol* **14**, 131-139.
- Curran, S., Strandkvist, C., Bathmann, J., de Gennes, M., Kabla, A., Salbreux, G. and Baum, B.** (2017). Myosin II Controls Junction Fluctuations to Guide Epithelial Tissue Ordering. *Dev Cell* **43**, 480-492 e486.
- Edelstein, A., Amodaj, N., Hoover, K., Vale, R. and Stuurman, N.** (2010). Computer control of microscopes using microManager. *Curr Protoc Mol Biol Chapter 14*, Unit14 20.
- Farhadifar, R., Roper, J. C., Aigouy, B., Eaton, S. and Julicher, F.** (2007). The influence of cell mechanics, cell-cell interactions, and proliferation on epithelial packing. *Curr Biol* **17**, 2095-2104.
- Fichelson, P., Brigui, A. and Pichaud, F.** (2012). Orthodenticle and Kruppel homolog 1 regulate *Drosophila* photoreceptor maturation. *Proc Natl Acad Sci U S A* **109**, 7893-7898.
- Freeman, M.** (1996). Reiterative use of the EGF receptor triggers differentiation of all cell types in the *Drosophila* eye. *Cell* **87**, 651-660.
- Garcia De Las Bayonas, A., Philippe, J. M., Lellouch, A. C. and Lecuit, T.** (2019). Distinct RhoGEFs Activate Apical and Junctional Contractility under Control of G Proteins during Epithelial Morphogenesis. *Curr Biol*.
- Giraldez, A. J., Perez, L. and Cohen, S. M.** (2002). A naturally occurring alternative product of the mastermind locus that represses notch signalling. *Mech Dev* **115**, 101-105.
- Grillo-Hill, B. K. and Wolff, T.** (2009). Dynamic cell shapes and contacts in the developing *Drosophila* retina are regulated by the Ig cell adhesion protein hibris. *Dev Dyn* **238**, 2223-2234.
- Heisenberg, C. P. and Bellaiche, Y.** (2013). Forces in tissue morphogenesis and patterning. *Cell* **153**, 948-962.
- Helms, W., Lee, H., Ammerman, M., Parks, A. L., Muskavitch, M. A. and Yedvobnick, B.** (1999). Engineered truncations in the *Drosophila* mastermind protein disrupt Notch pathway function. *Dev Biol* **215**, 358-374.
- Huang, J., Zhou, W., Dong, W., Watson, A. M. and Hong, Y.** (2009). From the Cover: Directed, efficient, and versatile modifications of the *Drosophila* genome by genomic engineering. *Proc Natl Acad Sci U S A* **106**, 8284-8289.
- Iwai, Y., Usui, T., Hirano, S., Steward, R., Takeichi, M. and Uemura, T.** (1997). Axon patterning requires DN-cadherin, a novel neuronal adhesion receptor, in the *Drosophila* embryonic CNS. *Neuron* **19**, 77-89.

- Johnson, R. I., Seppa, M. J. and Cagan, R. L.** (2008). The *Drosophila* CD2AP/CIN85 orthologue Cindr regulates junctions and cytoskeleton dynamics during tissue patterning. *J Cell Biol* **180**, 1191-1204.
- Koenig, J. H. and Ikeda, K.** (1983). Evidence for a presynaptic blockage of transmission in a temperature-sensitive mutant of *Drosophila*. *J Neurobiol* **14**, 411-419.
- Larson, D. E., Liberman, Z. and Cagan, R. L.** (2008). Cellular behavior in the developing *Drosophila* pupal retina. *Mech Dev* **125**, 223-232.
- LeGoff, L. and Lecuit, T.** (2015). Mechanical Forces and Growth in Animal Tissues. *Cold Spring Harbor perspectives in biology* **8**, a019232.
- Levayer, R. and Lecuit, T.** (2013). Oscillation and polarity of E-cadherin asymmetries control actomyosin flow patterns during morphogenesis. *Dev Cell* **26**, 162-175.
- Levayer, R., Pelissier-Monier, A. and Lecuit, T.** (2011). Spatial regulation of Dia and Myosin-II by RhoGEF2 controls initiation of E-cadherin endocytosis during epithelial morphogenesis. *Nat Cell Biol* **13**, 529-540.
- Leviten, M. W., Lai, E. C. and Posakony, J. W.** (1997). The *Drosophila* gene Bearded encodes a novel small protein and shares 3' UTR sequence motifs with multiple Enhancer of split complex genes. *Development* **124**, 4039-4051.
- Lienkamp, S. S., Liu, K., Karner, C. M., Carroll, T. J., Ronneberger, O., Wallingford, J. B. and Walz, G.** (2012). Vertebrate kidney tubules elongate using a planar cell polarity-dependent, rosette-based mechanism of convergent extension. *Nat Genet* **44**, 1382-1387.
- Munjal, A., Philippe, J. M., Munro, E. and Lecuit, T.** (2015). A self-organized biomechanical network drives shape changes during tissue morphogenesis. *Nature* **524**, 351-355.
- Ochoa-Espinosa, A., Harmansa, S., Caussinus, E. and Affolter, M.** (2017). Myosin II is not required for *Drosophila* tracheal branch elongation and cell intercalation. *Development* **144**, 2961-2968.
- Pare, A. C., Vichas, A., Fincher, C. T., Mirman, Z., Farrell, D. L., Mainieri, A. and Zallen, J. A.** (2014). A positional Toll receptor code directs convergent extension in *Drosophila*. *Nature* **515**, 523-527.
- Peifer, M. and Wieschaus, E.** (1990). The segment polarity gene armadillo encodes a functionally modular protein that is the *Drosophila* homolog of human plakoglobin. *Cell* **63**, 1167-1176.
- Perez-Mockus, G., Roca, V., Mazouni, K. and Schweisguth, F.** (2017). Neuralized regulates Crumbs endocytosis and epithelium morphogenesis via specific Stardust isoforms. *J Cell Biol* **216**, 1405-1420.
- Rauzi, M., Lenne, P. F. and Lecuit, T.** (2010). Planar polarized actomyosin contractile flows control epithelial junction remodelling. *Nature* **468**, 1110-1114.
- Ready, D. F., Hanson, T. E. and Benzer, S.** (1976). Development of the *Drosophila* retina, a neurocrystalline lattice. *Dev Biol* **53**, 217-240.
- Robertson, F., Pinal, N., Fichelson, P. and Pichaud, F.** (2012). Atonal and EGFR signalling orchestrate rok- and Drak-dependent adherens junction remodelling during ommatidia morphogenesis. *Development* **139**, 3432-3441.

- Royou, A., Sullivan, W. and Karess, R.** (2002). Cortical recruitment of nonmuscle myosin II in early syncytial *Drosophila* embryos: its role in nuclear axial expansion and its regulation by Cdc2 activity. *J Cell Biol* **158**, 127-137.
- Schindelin, J., Arganda-Carreras, I., Frise, E., Kaynig, V., Longair, M., Pietzsch, T., Preibisch, S., Rueden, C., Saalfeld, S., Schmid, B., et al.** (2012). Fiji: an open-source platform for biological-image analysis. *Nature methods* **9**, 676-682.
- Schweisguth, F.** (2004). Regulation of notch signaling activity. *Curr Biol* **14**, R129-138.
- Simoes Sde, M., Blankenship, J. T., Weitz, O., Farrell, D. L., Tamada, M., Fernandez-Gonzalez, R. and Zallen, J. A.** (2010). Rho-kinase directs Bazooka/Par-3 planar polarity during *Drosophila* axis elongation. *Dev Cell* **19**, 377-388.
- Simoes Sde, M., Mainieri, A. and Zallen, J. A.** (2014). Rho GTPase and Shroom direct planar polarized actomyosin contractility during convergent extension. *J Cell Biol* **204**, 575-589.
- Singh, J. and Mlodzik, M.** (2012). Hibris, a *Drosophila* nephrin homolog, is required for presenilin-mediated Notch and APP-like cleavages. *Dev Cell* **23**, 82-96.
- Tetley, R. J., Blanchard, G. B., Fletcher, A. G., Adams, R. J. and Sanson, B.** (2016). Unipolar distributions of junctional Myosin II identify cell stripe boundaries that drive cell intercalation throughout *Drosophila* axis extension. *Elife* **5**.
- Thevenaz, P., Ruttimann, U. E. and Unser, M.** (1998). A pyramid approach to subpixel registration based on intensity. *IEEE Trans Image Process* **7**, 27-41.
- Trylinski, M., Mazouni, K. and Schweisguth, F.** (2017). Intra-lineage Fate Decisions Involve Activation of Notch Receptors Basal to the Midbody in *Drosophila* Sensory Organ Precursor Cells. *Curr Biol* **27**, 2239-2247 e2233.
- Tseng, Q., Duchemin-Pelletier, E., Deshiere, A., Balland, M., Guillou, H., Filhol, O. and Thery, M.** (2012). Spatial organization of the extracellular matrix regulates cell-cell junction positioning. *Proc Natl Acad Sci U S A* **109**, 1506-1511.
- Weinmaster, G. and Fischer, J. A.** (2011). Notch ligand ubiquitylation: what is it good for? *Dev Cell* **21**, 134-144.
- Wolff, T. and Ready, D. F.** (1991). Cell death in normal and rough eye mutants of *Drosophila*. *Development* **113**, 825-839.
- Wolff., T. a. R., D.F.** (1993). Pattern formation in the *Drosophila* retina. In *The Development of Drosophila melanogaster* (ed. C. S. H. Press), pp. 1277-1325. NY: Cold Spring Harbor.
- Yin, C., Kiskowski, M., Pouille, P. A., Farge, E. and Solnica-Krezel, L.** (2008). Cooperation of polarized cell intercalations drives convergence and extension of presomitic mesoderm during zebrafish gastrulation. *J Cell Biol* **180**, 221-232.

- Yoshida-Noro, C., Suzuki, N. and Takeichi, M.** (1984). Molecular nature of the calcium-dependent cell-cell adhesion system in mouse teratocarcinoma and embryonic cells studied with a monoclonal antibody. *Dev Biol* **101**, 19-27.
- Zallen, J. A. and Wieschaus, E.** (2004). Patterned gene expression directs bipolar planar polarity in *Drosophila*. *Dev Cell* **6**, 343-355.

Figures

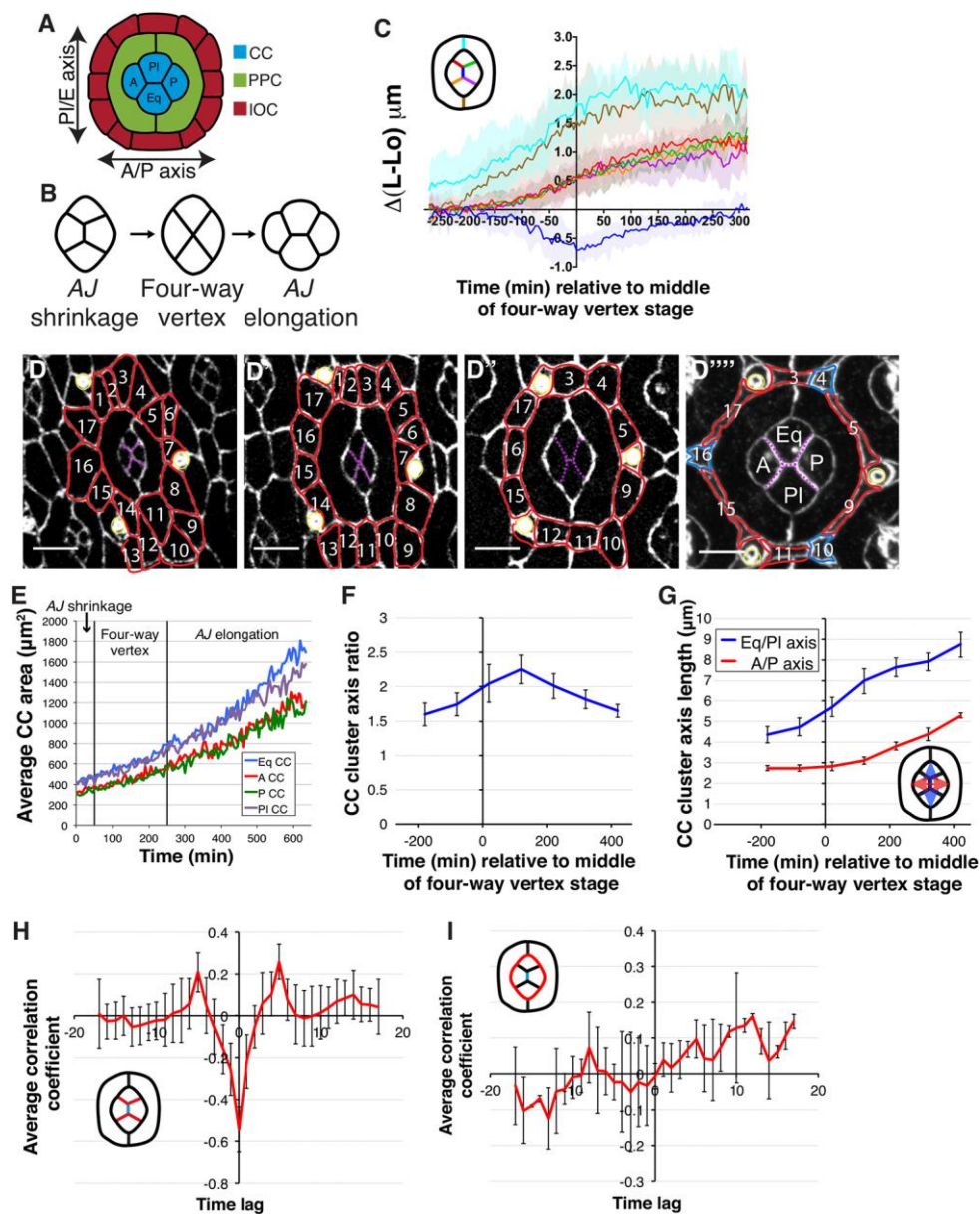


Figure 1: Cone cell intercalation and retinal cell growth trajectories.

(A) The arrangement of cells in the ommatidium. (B) Stages of intercalation of the cone cells. (C) Average relative length (L-L0) of cone and primary pigment cell AJs during ommatidium development. Time 0 is middle of the four-way vertex stage (n=13 ommatidia from 2 retinas). (D) Confocal sections taken from a time-lapse movie of ommatidium development, with AJs labeled with endogenous Ecad::GFP. Interommatidial cells are outlined in red and numbered through subsequent frames. Tertiary pigment cells are labeled in blue. (E) Average apical area of cone cells over

time (n=4 ommatidia). Vertical lines demarcate the stages of cone cell intercalation. **(F)** Average cone cell cluster axis ratio over time relative to the middle of the four-way vertex stage (n=14 ommatidia). **(G)** Average cone cell cluster axes lengths over time relative to the middle of the four-way vertex stage (n=14 ommatidia). **(H)** Average cross-correlation of rate of change in the length of the central cone cell AJ (shown in blue in the schematic), with the adjoining cone cell AJs (shown in red in the schematic). Correlation coefficient: $r=-0.54\pm 0.11$ (mean \pm S.D.) at a time lag of 0 (n=13 ommatidia). **(I)** Average cross-correlation of rate of change in length of the central cone cell AJ (shown in blue in the schematic) with the cone-primary pigment cell AJ (shown in red in the schematic) (n=13 ommatidia). Scale bars = 5 μ m. Error bars = S.D.

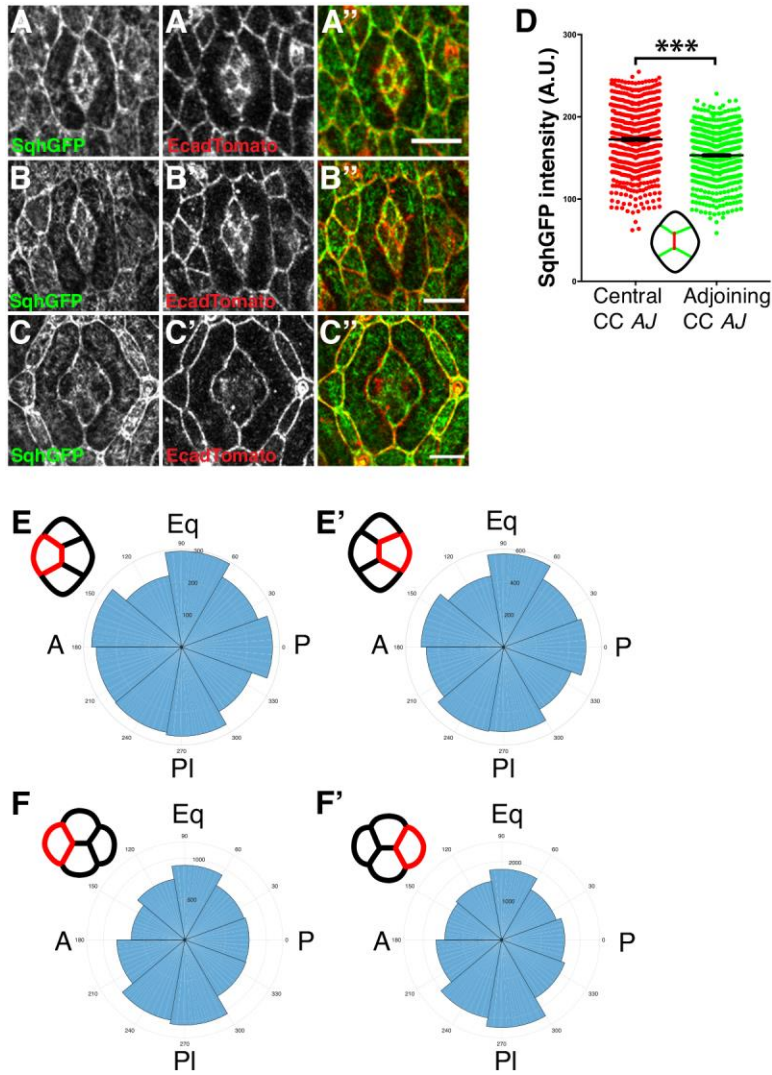


Figure 2: MyoII expression and dynamics in cone cell intercalation.

(A-C) *sqh^{AX3};sqh-sqh::GFP/+;Ecad::Tomato/+* flies showing localization of MyoII (Sqh::GFP) at the junction shrinkage **(A)**, four-way vertex **(B)** and junction elongation **(C)** stages of cone cell intercalation. **(D)** Quantification at the AJ shrinkage stage of Sqh::GFP intensity on shrinking A/P cone cell AJ compared to adjoining AJs paired by ommatidium (n=514 ommatidia). Paired T-test: $p < 0.0001$. **(E-F)** Polar histograms showing directions of MyoII flow vectors calculated by PIV. **(E)** A and **(E')** P cone cells during AJ shrinkage phase. **(F)** A and **(F')** P cone cells during AJ elongation phase. Scale bars = 5 μ m. Error bars = S.E.M.

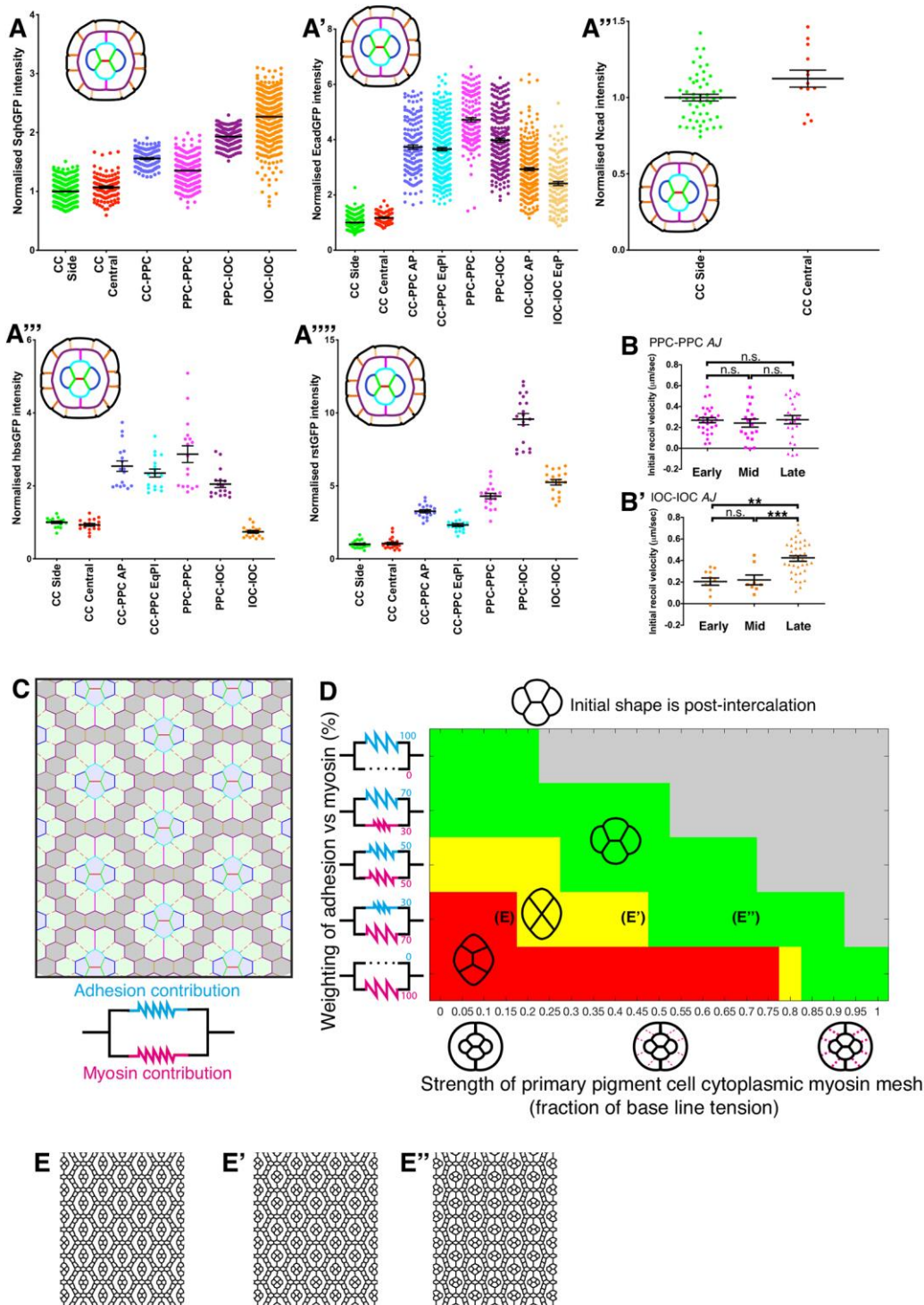


Figure 3: Modeling the contribution of MyoII contractility and adhesion in cone cell intercalation.

(A-A''') Quantification at AJ elongation stage of (A) Sqh::GFP, (A') Ecad::GFP, (A'') Ncad staining, (A''') Hbs::GFP intensity, and (A''') Rst::GFP intensity on each AJ type normalized to the average of the cone cell-cone cell side AJ (shown in green). (B-B')

Initial recoil velocity of ablation of **(B)** Primary pigment-primary pigment cell AJs and **(B')** interommatidial-interommatidial cell AJs at each stage of ommatidial development. For primary pigment-primary pigment cell AJs: one-way ANOVA n.s. $p=0.784$, $n=29, 20, 24$ AJs respectively. For interommatidial-interommatidial cell AJs: one-way ANOVA $p<0.0001$, Tukey's post hoc: Early-Mid n.s. $p=0.97$, Early-Late $p=0.0001$, Mid-Late $p=0.0018$. $n=11, 8, 38$ AJs respectively. **(C)** Each cell-cell boundary included in the vertex model is color-coded following the code used in **(A-B)**. The bonds representing the cytosolic contractile actomyosin meshworks are represented as dashed magenta lines, with the cone cells highlighted in blue, primary pigment cells in green and interommatidial cells in grey. The parallel spring schematic represents the tension structure for adhesion and myosin contribution in each cell-cell contact. **(D)** Heatmap demonstrating the state of intercalation as a function of cytosolic contractile actomyosin meshwork strength (as a fraction of base tension level) (x-axis) and the range of contributions from adhesion and myosin intensity measurements (y-axis). Spring schematics represent the weight of each adhesion and MyoII in calculation of tension values for each row. Ommatidia schematics represent the strength of the cytosolic mesh. See Methods and Supplementary Table 1 for details. Green represents stable intercalation (shown in **E''**), red represents failed intercalation, shown in **(E)** and yellow represents a stable 4-way junction forming a rosette, shown in **(E')**. Grey points have unstable ommatidia geometry. **(E-E'')** Simulation snapshots where the tension values cannot drive or stabilize the intercalation **(E)**, where a stable 4-way junction is formed **(E')**, and where a stable intercalation occurs **(E'')**. Error bars = S.E.M.

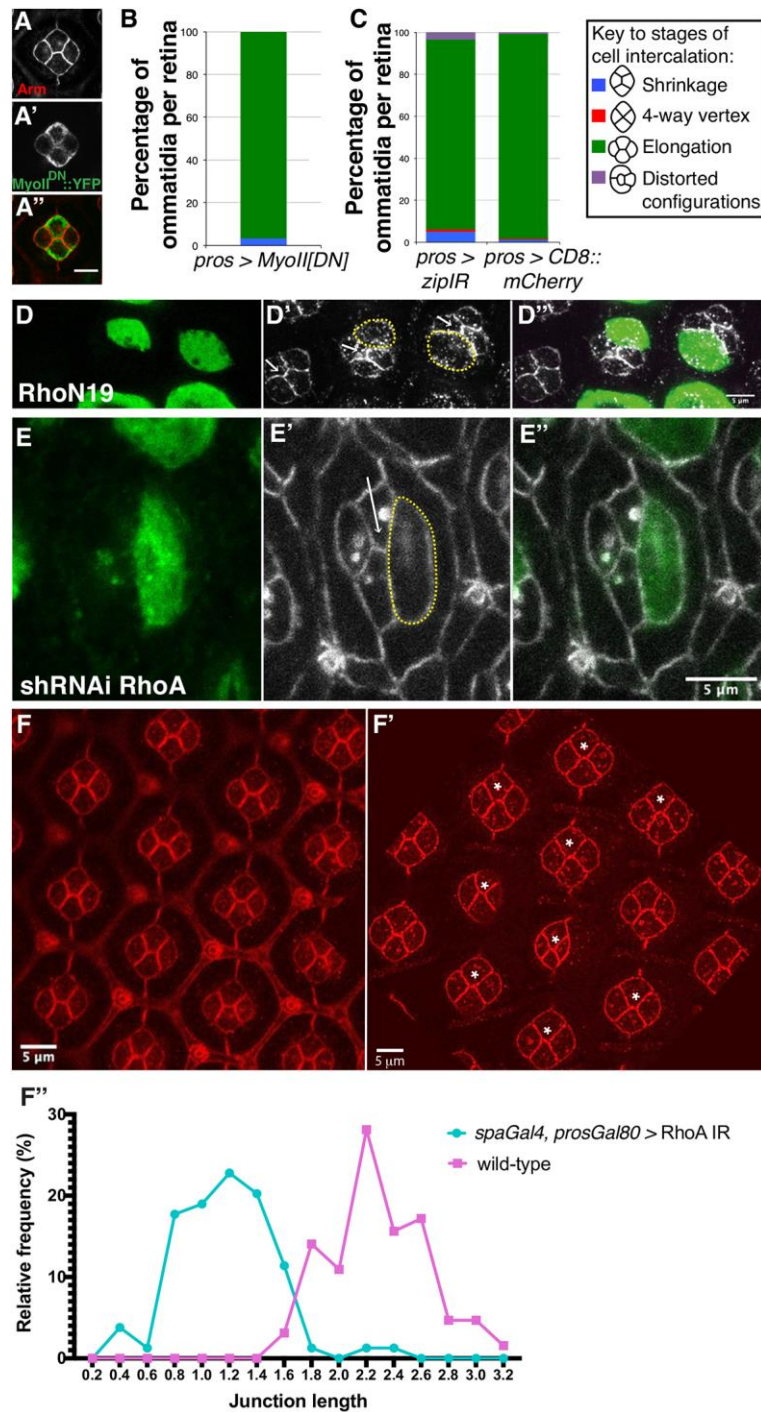


Figure 4: The RhoA-MyoII pathway is largely dispensable for cone cell intercalation

(A) *UAS-MyoII^{DN}::YFP* expressed under control of *pros-Gal4*. (B) Progression of cone cell intercalation at 29°C when MyoII^{DN} is expressed in the cone cells (n=4 retinas, 2212 ommatidia). (C) Progression of cone cell intercalation for *UAS-zip1R* expressed

under control of *pros-Gal4* alongside matched controls expressing *UAS-CD8::mCherry*, raised at 29°C. (*pros-Gal4; zip1R*: n=6 retinas, controls: n=4 retinas). 'Other' category contains any cone cell orientations that do not fit into the other categories e.g. shift in position of the primary pigment cell junctions relative to the cone cells. **(D)** GFP-positive cells (circles using a dashed yellow line) express the *RhoA^{N19}* transgene. White arrows point to the newly extended AJ between the Polar and Equatorial cone cells **(E)** GFP-positive cells (circles using a dashed yellow line, n=15) express an *shRhoA* RNAi transgene. White arrows point to the newly extended AJ between the Polar and Equatorial cone cells **(F)** wild-type, and **(F')** *spaGal4, prosGal80* genotype to express the *shRhoA* RNAi in the primary pigment cells. Ommatidia marked with a (*) show a shorter AJ between the Polar and equatorial cone cells, when compared to wild type. The length of these AJs is quantified in **(F'')**. 3 retinas; *spaGal4, prosGal80* n=80 and control n=65. Scale bars: **(A)** = 5µm, **(D'')** = 10µm.

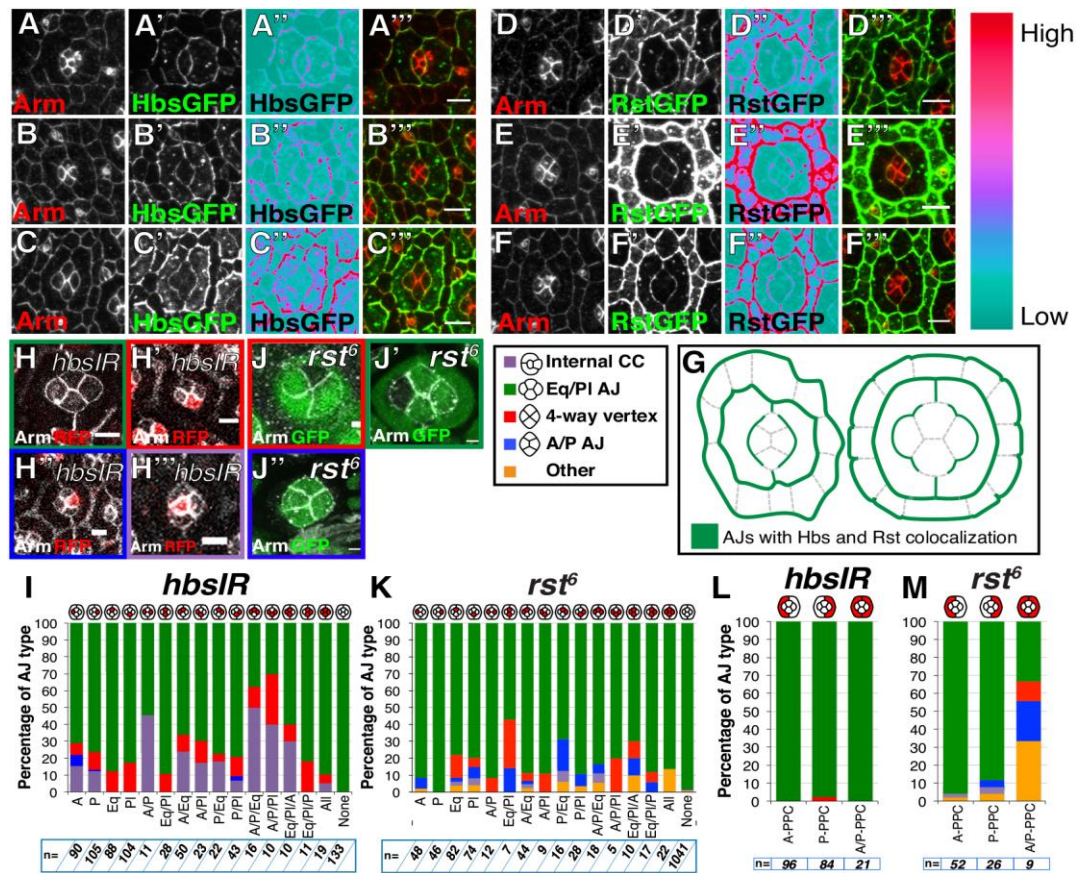


Figure 5: Roughest and Hibris regulate cone cell intercalation.

(A-F) Confocal projection through the cone cells showing **(A-C)** Hbs::GFP and **(D-F)** Rst::GFP at **(A,D)** AJ shrinking stage, **(B,E)** four-way vertex stage and **(C,F)** AJ elongation stage. **(A'',B'',C'',D'',E'',F'')** LUT to visualize variation in levels along the cone-primary pigment cell AJ. Note the reduction in intensity around the PI and Eq cone cells. **(G)** Schematic depicting where Hbs and Rst colocalize. **(H)** Representative wildtype, control ommatidium from a *hbsIR* mosaic retina **(H')** Eq cell expressing *hbsIR* (red) and stalled at the four-way vertex **(H'')** P cone cell expressing *hbsIR* and stalled at the shrinking stage **(H''')** Anterior cone cell expressing *hbsIR* and showing a cell sorting phenotype. **(I)** Quantification of cone cell intercalation in *hbsIR* mosaic ommatidia. shRNAi expressing cells are color coded (red). **(J)** PI cone cell mutant for *rst⁶* (lacking GFP) stalled at the 4-way vertex. **(J')** A cone cell mutant for *rst⁶* (lacking GFP) undergoes normal intercalation. **(J'')** Primary pigment cells

mutant for *rst*^δ (lacking GFP) fail to shrink the A/P cone cell AJ. **(K-M)** Quantification of cone cell intercalation in mosaic ommatidia. shRNAi for *hbs* and *rst*^δ mutant cells are color coded (Red).

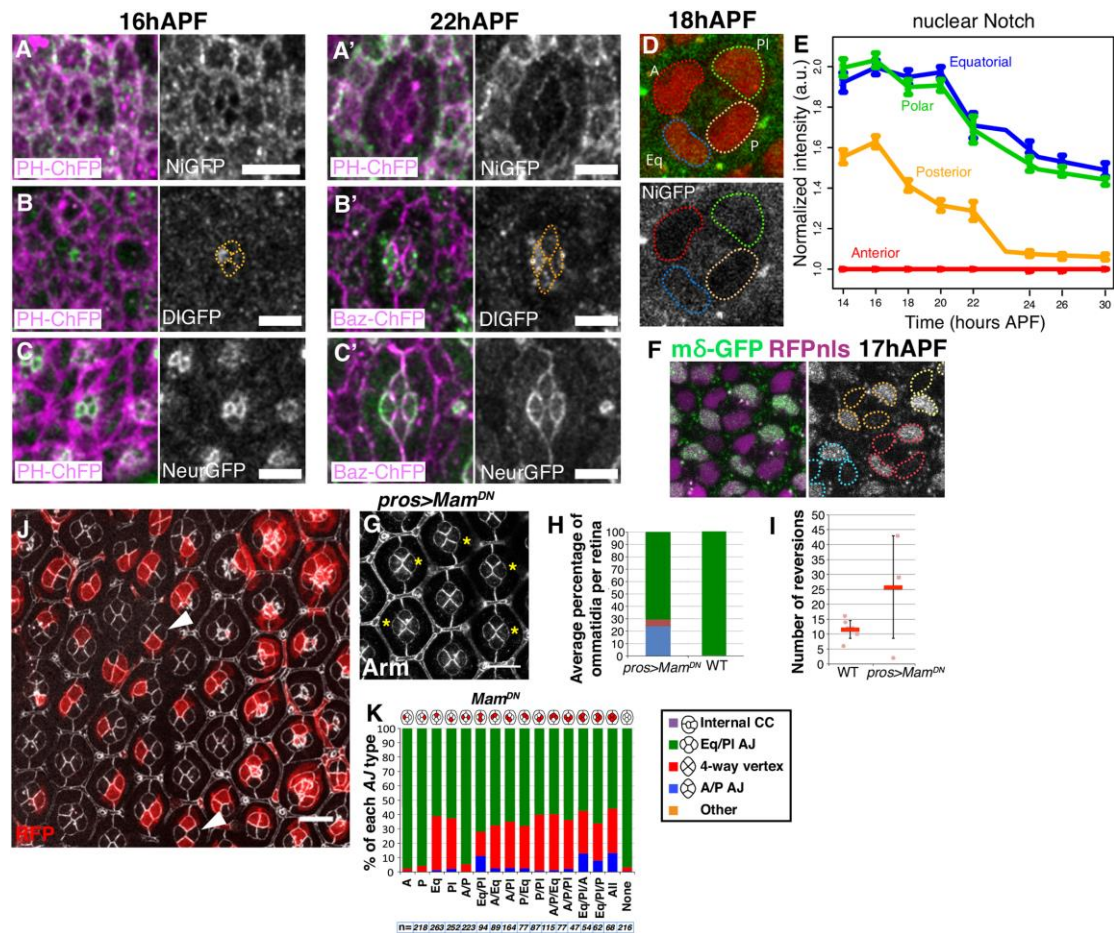


Figure 6: Notch signaling controls cone cell intercalation.

(A-A') Time-course of NiGFP expression (grey) during cone cell intercalation. Cell membranes are labeled with PH::ChFP (Purple). **(B-B')** Time-course of DI::GFP expression (grey) during cone cell intercalation. The cone cells are outlined using a dashed, orange line. Cell membranes are labeled with PH::ChFP (Purple) in **(B)** and with Baz::ChFP in **(B')**. **(C-C')** Time-course of Neur::GFP expression (grey) during cone cell intercalation. Cell membranes are labeled with Baz::ChFP (Purple). **(D)** Representative NiGFP signal (grey) in the cone cell nuclei, also labeled using an RFP-nls reporter (red). **(E)** Quantification of the nuclear signal for N in the cone cells over time. Note the drop in N signal in the P cell as intercalation takes place. **(F)** Representative staining of the N target gene $m\delta$ -GFP (grey). Cone cell nuclei are labeled using an RFP-nls reporter (purple) and are circled using colored dashed lines with one specific color attributed per quartet. **(G)** $UAS-Mam^{DN}$ expressed under

control of *prosGal4*. **(H)** Progression of cone cell intercalation for retinas expressing *UAS-Mam^{DN}* under control of *prosGal4* (n=5 retinas, 3433 ommatidia) and for control wild type flies raised at 25°C (n=3 retinas, 1909 ommatidia). **(I)** Number of reversions between the different stages of cone cell intercalation in wild type compared to *UAS-Mam^{DN}/pros-Gal4* retinas (WT n=8 ommatidia, *pros>Mam^{DN}* n=4 ommatidia). **(J)** Single cells expressing *UAS-Mam^{DN}* marked by presence of RFP. Arrowheads indicate examples of cone cells at a four-way vertex stage when the Eq cell is affected and quartet with a A/P AJ when the Eq and PI cone cells are affected. **(K)** Quantification of the percentage of ommatidia with each AJ type (A/P, four-way vertex, Eq/PI) when different combinations of cone cells express *UAS-Mam^{DN}*. N numbers are shown with each panel. Scale bars: **(A-C)** = 5µm, **(G,J)** = 10µm. Error bars: **(E, I)** = S.D.

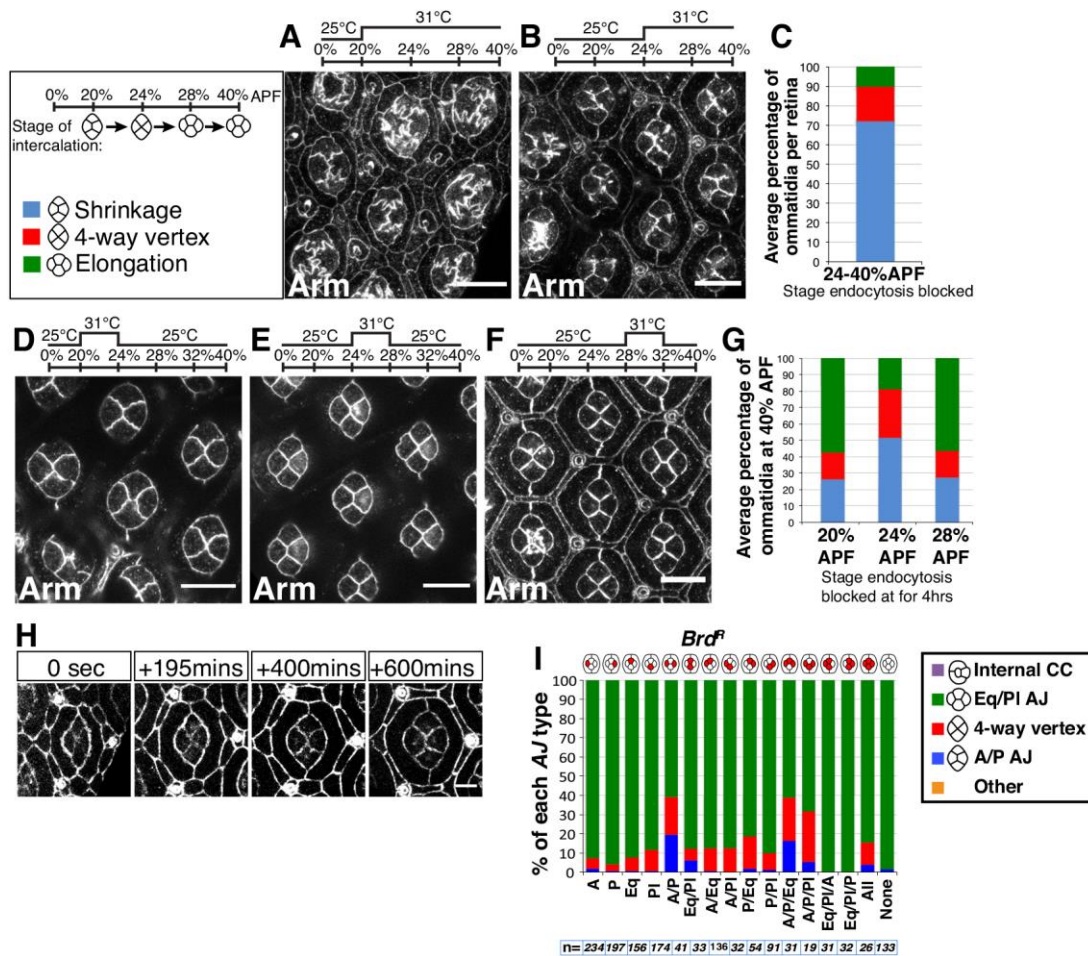
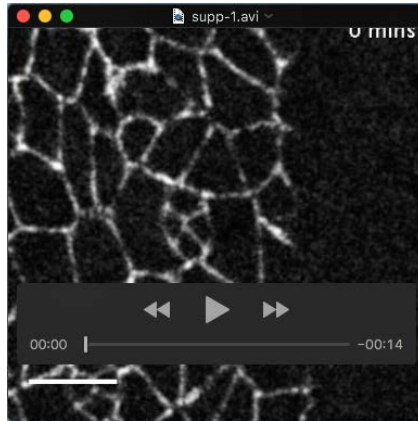


Figure 7: Endocytosis plays a role at all steps of cone cell intercalation.

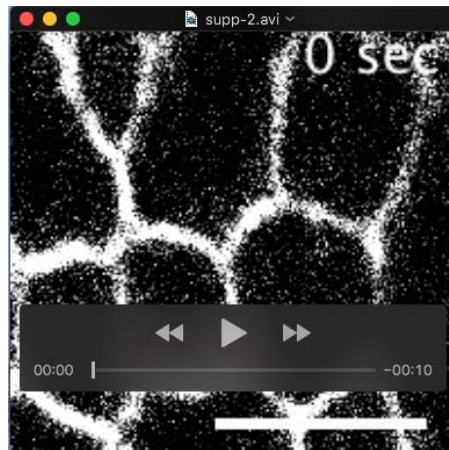
(A-B, D-F) Retinas expressing *UAS-shibire^{ts}* under the control of *prosGal4* stained for Arm. Flies were raised at 25°C and then transferred to 31°C at **(A)** 20%APF, **(B)** 24%APF and incubated O/N. Flies were transiently transferred to restrictive temperature for 4hrs at **(D)** 20%APF, **(E)** 24%APF and **(F)** 28%APF. **(C)** Progression of cone cell intercalation in **(B)** (n=4 retinas, 1442 ommatidia). **(G)** Progression of cone cell intercalation in **(D-F)** (n=7, 6, 6 retinas respectively; 3352, 3100, 2797 ommatidia respectively). **(H)** Stills taken from a movie of retina expressing *UAS-shibire^{ts}* under the control of *prosGal4* with *Ecad::GFP* to label the AJs. Cone cell AJs are overlaid in red. **(I)** Quantification of the percentage of ommatidia with each AJ type (A/P, four-way vertex, Eq/PI) when different combinations of cone cells express *UAS-Brd^R*. Scale bars: **(A-B, D-F)** = 10µm, **(H)** = 5µm.

Table S1

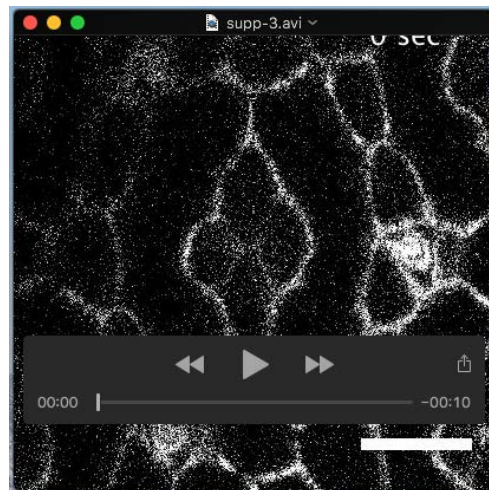
Cell type	Ideal area as a fraction of $A^{(0)}_{\alpha}$			
	Post-intercalation			
Pigment cell (PPC)	8.7			
Cone cell (CC) sides	1			
Cone cell (CC) top/bottom	1.3			
(IOCs)	1			
Contact type	Post- intercalation			
	c_{ad}	c_{myo}	S if $w_{ad} = 1$ $w_{myo} = 0$	S if $w_{ad} = 0$ $w_{myo} = 1$
CC-CC side contact	1.00	1.00	1.00	1.00
CC-CC central contact	1.08	1.06	0.93	1.06
CC – PPC (Eq/Pl)	1.79	1.52	0.56	1.52
CC – PPC (A/P)	2.11	1.52	0.47	1.52
PPC-PPC contact	3.25	1.33	0.31	1.33
PPC - IOC contact	4.83	1.93	0.21	1.93
IOC-IOC (A/P)	2.37	2.24	0.19*	1.33*
IOC-IOC (Eq/Pl)	2.24	2.30	0.29*	2.02*
all else	1.00	1.00	1.00	1.00



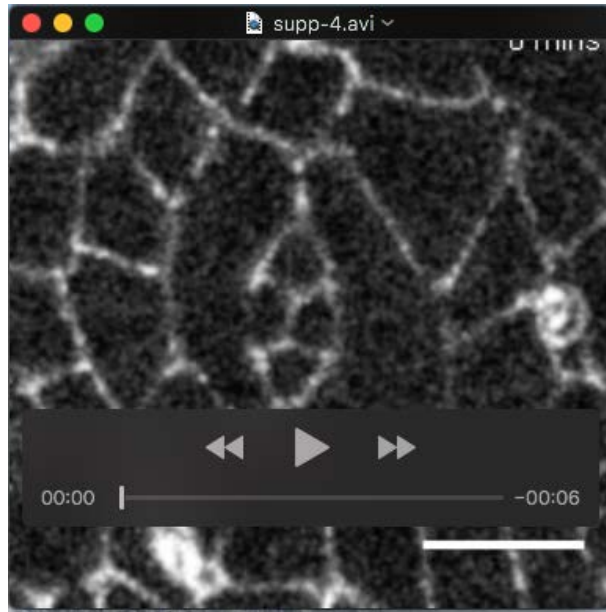
Movie 1: Time-lapse of a representative cone cell intercalation. Cells are labeled using Ecad::GFP. Frame interval = 5 minutes. Scale bar = 5 μ m.



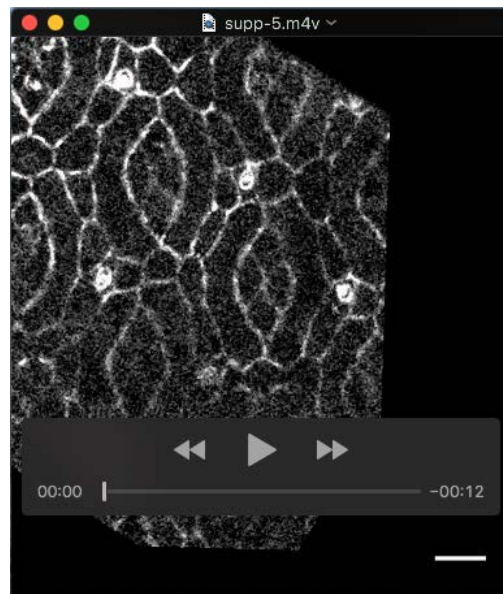
Movie 2: Representative laser ablation of an inter-Interommatidial cell AJ. Cells are labeled using Ecad::GFP. Frame interval = 1 second. Scale bar = 5 μ m.



Movie 3: Representative laser ablation of an Inter-primary pigment cell AJ. Cells are labeled using Ecad::GFP. Frame interval = 1 second. Scale bar = 5 μ m.



Movie 4: Representative cone cell quartet expressing Mam^{DN}. Cells are labeled using Ecad::GFP. Frame interval = 5 minutes. Scale bar = 5 μ m.



Movie 5: Time-lapse of a representative cone cell intercalation upon endocytosis inhibition. Cells are labeled using Ecad::GFP. Movie starts at a timepoint when in WT the majority of cone cells would be at the four-way vertex and would expand their Eq/PI junctions. Note how when endocytosis is blocked, intercalation is stalled or cone cells even revert their contacts. Frame interval = 10 min. Scale bar = 5 μ m.

e 1: fluctuations in AJ length

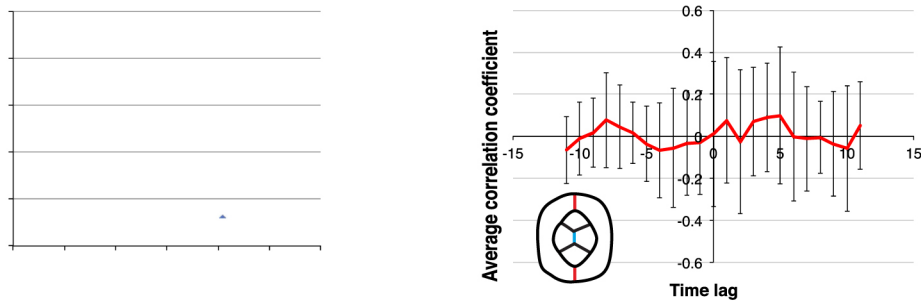


Figure S1: Fluctuations in AJ length.

(A) Length of central cone cell AJ and the primary pigment cell AJs of one ommatidium showing negative correlation. Pearson's correlation coefficient for this example: $r=-0.74$ for PI primary-primary cell and $r=-0.67$ for Eq primary-primary pigment cell. Average correlation coefficient: $r=-0.6\pm 0.19$ (mean \pm S.D.) ($n=13$ ommatidia). **(B)** Average cross-correlation of rate of change in the length of the central cone-cone AJ (shown in blue in schematic) with the primary-primary AJs (shown in red in schematic) ($n=13$ ommatidia). Error bars = S.D.

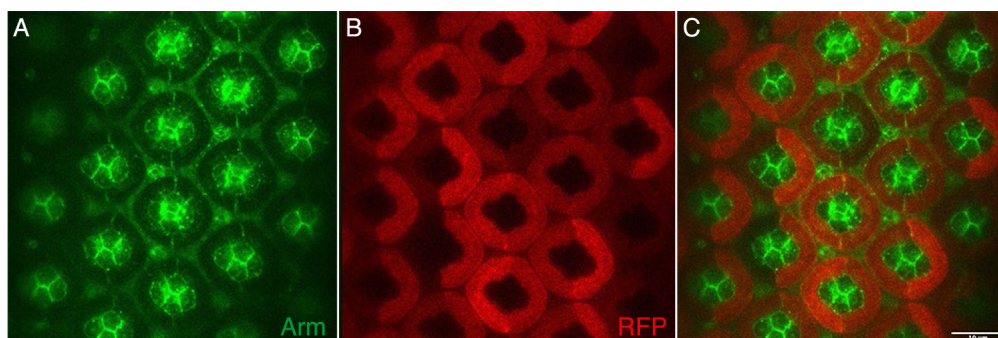


Figure S2: Specific transgene expression in the primary pigment cells. The *spaGal4*, *prosGal80* strain allows specific expression of a *UAS-RFP* transgene in the primary pigment cells.